

## LY $\alpha$ RADIATION FROM COLLAPSING PROTOGALAXIES I: CHARACTERISTICS OF THE EMERGENT SPECTRUM.

MARK DIJKSTRA<sup>1,3</sup>, ZOLTÁN HAIMAN<sup>1</sup> & MARCO SPAANS<sup>2</sup>

<sup>1</sup>Department of Astronomy, Columbia University, 550 West 120th Street, New York, NY 10027

<sup>2</sup>Kapteyn Astronomical Institute, P.O. Box 800, 9700 AV Groningen, The Netherlands

<sup>3</sup>School of Physics, University of Melbourne, Victoria 3010, Australia

*Draft version December 30, 2018*

### ABSTRACT

We present Monte Carlo calculations of Ly $\alpha$  radiative transfer through optically thick, spherically symmetric, collapsing gas clouds. These represent simplified models of proto-galaxies that are caught in the process of their assembly. Such galaxies produce Ly $\alpha$  flux over an extended solid angle, either from a spatially extended Ly $\alpha$  emissivity, or from scattering effects, or both. We present a detailed study of the effect of the gas distribution and kinematics, and of the Ly $\alpha$  emissivity profile, on the emergent spectrum and surface brightness distribution. The emergent Ly $\alpha$  spectrum is typically double-peaked and asymmetric. In practice, however, we find that the blue peak is significantly enhanced and the red peak, in most cases, will be undetectable. This results in an effective blueshift, which, combined with scattering in the intergalactic medium, will render extended Ly $\alpha$  emission from collapsing protogalaxies difficult to detect beyond redshift  $z \gtrsim 4$ . We find that the surface brightness distribution is typically flat, and that a strong wavelength dependence of its slope (with preferential flattening at the red side of the line) would be a robust indication that Ly $\alpha$  photons are being generated (rather than just scattered) in a spatially extended region around the galaxy, as in the case of a cooling flow. We also find that for self-ionized clouds whose effective Ly $\alpha$  optical depth is  $\lesssim 10^3$ , infall and outflow models can produce nearly identical spectra and surface brightness distributions, and are difficult to distinguish from one another. The presence of deuterium with a cosmic abundance may produce a narrow but detectable dip in the spectra of systems with moderate hydrogen column densities, in the range  $10^{18} - 10^{20} \text{ cm}^{-2}$ . Finally, we present a new analytic solution for the emerging Ly $\alpha$  spectrum in the limiting case of a static uniform sphere, extending previous solutions for static plane-parallel slabs.

*Subject headings:* galaxies: formation – galaxies: halos – quasars: general – radiative transfer – cosmology: theory – intergalactic medium

### 1. INTRODUCTION

Ly $\alpha$  radiation is an inevitable ingredient of galaxy formation. In the standard cosmogony of hierarchical structure formation, potential wells created by gravitationally bound dark matter form the seeds of galaxies. Gas cools and settles inside its host dark matter halo, radiating away most of its gravitational binding energy. In dark matter halos with  $T_{\text{vir}} > 10^4$  K, the majority of this radiation can emerge in the Ly $\alpha$  line (Haiman et al. 2000; Fardal et al. 2001). Detecting this gravitational cooling radiation would shed light on the distribution and dynamics of gas in galaxies, in their ‘protogalactic phase’. This refers to the early phase in the evolution of a galaxy, likely prior to its first epoch of significant star formation.

At the onset of star formation the total Ly $\alpha$  flux from collapsing gas clouds may be boosted; photo-ionization and subsequent recombination converts  $\sim$  two of every three ionizing photons produced by these sources into Ly $\alpha$ . Since only young massive stars are capable of producing (substantial) ionizing radiation, Ly $\alpha$  emission is associated with star-forming regions. For this reason, strong Ly $\alpha$  emission is expected from young galaxies (Partridge & Peebles 1967). However, if stars only form when the overall gas distribution has collapsed significantly, then this boost in Ly $\alpha$  emission is only achieved at a later stage in the formation of a galaxy. On the other hand, a quasar may be in place at a much earlier stage of the collapse of the gas (see Haiman 2004). A (luminous) central quasar has the ability to increase the total Ly $\alpha$  flux from a spatially extended protogalactic gas cloud by several orders of magnitude (Haiman & Rees 2001). Illumination by a central quasar thus may give rise to enhanced Ly $\alpha$  emission from gas in the protogalactic

phase, which may spatially extend to  $\gtrsim 100$  kpc, subtending a solid angle exceeding  $100 \text{ arcsec}^2$ .

Based on the three Ly $\alpha$  emission mechanisms sketched above – cooling radiation, or recombination powered by the ionizing radiation of stars or quasar black holes, – copious Ly $\alpha$  emission is expected from the early stages of galaxy formation. Simple estimates of the total Ly $\alpha$  line flux show that it can be detectable with modern instruments out to high redshifts. However, quantifying the properties of Ly $\alpha$  radiation emerging from protogalaxies, such as its expected surface brightness profile and spectral energy distribution, is fraught with difficulties: (i) it is not well understood how and where the Ly $\alpha$  photons are generated, (ii) the optical depth  $\tau$  in the line exceeds unity for columns of neutral hydrogen  $\gtrsim 10^{14} \text{ cm}^{-2}$ , so that protogalaxies are expected to be optically thick with  $\tau \gtrsim 10^3$ , necessitating computationally expensive radiative transfer calculations, and (iii) complex gas density and velocity distributions (e.g. Kunth et al. 1998), as well as the presence of dust (e.g. Neufeld 1991; Charlot & Fall 1993; Hansen & Oh 2005), complicate any simplified predictions. Additionally, at redshifts  $z \gtrsim 3$ , the intergalactic medium (IGM) is optically thick at the Ly $\alpha$  frequency, and will modify the observed spectrum.

Previous works have calculated the properties of the Ly $\alpha$  radiation emerging from galaxies under various simplified conditions, including treatment of Ly $\alpha$  radiative transfer in optically thick media analytically (Harrington 1973; Neufeld 1990), numerically (Unno 1952; Field 1959; Adams 1972), or more recently using Monte-Carlo methods (e.g. Ahn et al. 2000, 2002; Zheng & Miralda-Escudé 2002; Cantalupo et al. 2005; Hansen & Oh 2005). Here we employ Monte Carlo simulations simi-

lar to those used in previous papers, but our study differs from preceding work in several ways. We focus on the generation of extended Ly $\alpha$  emission in the earliest stages of galaxy formation, when there is still significant gas infall with an extended spatial distribution. Therefore, the geometry we study is that of a spherically symmetric, collapsing gas cloud, with different radial density and velocity profiles. In addition, we explore a wide range of intrinsic Ly $\alpha$  emissivity profiles that may be appropriate for the earliest galaxies. In each case, we provide detailed explanations of the characteristics of the emergent spectrum.

Our study was motivated in part by recent observations. The flux levels expected from protogalaxies have now been reached in large Ly $\alpha$  surveys. Wide-field narrow-band surveys, such as for example the Large Area Lyman Alpha (LALA) survey (Rhoads et al. 2000) carried out on Kitt Peak, with spectroscopic follow up done on Keck and a similar survey on Subaru (e.g. Hu et al. 2004) have been very fruitful in finding galaxies at redshifts  $z = 4.5$  (e.g. Malhotra & Rhoads 2002; Dawson et al. 2004),  $z = 5.7$  (Rhoads & Malhotra 2001; Ajiki et al. 2003; Hu et al. 2004; Ouchi et al. 2005) and 6.5 (Kodaira et al. 2003; Rhoads et al. 2004) albeit at lower flux levels than initially predicted by Partridge & Peebles (1967).

Although the majority of the observed Ly $\alpha$  emitters appear point-like (within the detection limits), several tens of extended Ly $\alpha$  sources have currently been observed at  $z \sim 3$  (e.g. Steidel et al. 2000; Matsuda et al. 2004). Only in a few cases are the ionization or excitation mechanisms known. Bunker et al. (2003) found spatially extended Ly $\alpha$  emission around a  $z \sim 4.5$  quasar. Because continuum emission from stars could not be found, Bunker et al. (2003) suggest that no star formation has taken place in this illuminated gas cloud, and that it is still in its early protogalactic phase. Evidence for gas infall onto quasars has also been found by Barkana & Loeb (2003) as an absorption feature in the quasar's Ly $\alpha$  emission line. More recently, Weidinger et al. (2004, 2005) found extended Ly $\alpha$  emission from pristine (not polluted by metals) gas around a  $z \sim 3$  quasar. The absence of metals is by itself very suggestive that no significant star formation has taken place in the cloud. Additionally, Weidinger et al. (2004, 2005) claim that their combination of deep imaging and spectroscopy allows a determination of the gas' velocity field, which is consistent with spatially extended collapsing gas. The physical picture that emerges from these observations point strongly towards the collapse of protogalactic gas (also see Haiman 2004; Haiman & Quataert 2004). A similar extended Ly $\alpha$  "fuzz" has been discovered around 4 additional quasars recently by Christensen (2005).

Future searches for both Ly $\alpha$  emitters and blobs will undoubtedly reveal more Ly $\alpha$  emitters, point-like and extended. Deeper observations and/or higher resolution spectra may contain detailed information on the gas distribution and kinematics. Therefore, it is timely to ask the following questions: *Given a high signal-to-noise Ly $\alpha$  surface brightness profile and/or spectrum, what can we learn about the excitation/ionization mechanism creating the Ly $\alpha$  photons and about the properties of the gas through which the Ly $\alpha$  is propagating?* To properly address these questions, the radiative transfer of the Ly $\alpha$  out of these (proto) galaxies needs to be understood.

In this paper, we present Monte Carlo computations of Ly $\alpha$  transfer through models of protogalactic gas configurations. The main goal is to gain basic insights into the properties of the emerging Ly $\alpha$  radiation, and into how these properties depend

on the assumed gas density distribution, gas kinematics and on where the Ly $\alpha$  is generated. Furthermore, we study how these predictions change in the presence of an ionizing source. The current paper focuses on spherically symmetric gas configurations, which is obviously oversimplified. However, the absence of complicated geometrical effects makes our results easier to interpret and may fulfill the same role for (future), more sophisticated 3-D simulations, that analytic solutions have played for the present work. In a companion paper (Dijkstra et al. 2005, hereafter Paper II), we present a detailed comparison of our models with several existing observations of Ly $\alpha$  emitters.

The rest of this paper is organized as follows. In § 2, we briefly review the basics of Ly $\alpha$  transfer. In § 3, we describe our code, along with several tests we performed to check its accuracy. In § 4, we describe how deuterium was included in our calculations, and a motivation for why and when this is relevant. In § 5, we apply our code to transfer calculations of neutral collapsing gas clouds. In § 6, we present our main results on the emergent spectra and surface brightness profiles. In § 7, we investigate the additional effect of an embedded ionizing source. In § 8, we discuss potential caveats in our calculations. Finally, in § 9, we present our conclusions and summarize the potential implications of this work. The parameters for the background cosmology used throughout this paper are  $\Omega_m = 0.3$ ,  $\Omega_\Lambda = 0.7$ ,  $\Omega_b = 0.044$ ,  $h = 0.7$ , based on Spergel et al. (2003).

## 2. LY $\alpha$ RADIATIVE TRANSFER BASICS

The basics of transfer of Ly $\alpha$  resonance line radiation has been the subject of research for many decades and is well understood (e.g. Unno 1952; Field 1959; Adams 1972; Harrington 1973; Neufeld 1990). The goal of this section is to review the basics of Ly $\alpha$  scattering, relevant to understanding this paper. It is convenient to express frequencies  $\nu$  in terms of  $x \equiv (\nu - \nu_0)/\Delta\nu_D$ , where  $\Delta\nu_D = v_{th}\nu_0/c$ , and  $v_{th}$  is the thermal velocity of the hydrogen atoms in the gas, given by  $v_{th} = \sqrt{2k_B T/m_p}$ , where  $k_B$  is the Boltzmann constant,  $T$  the gas temperature,  $m_p$  the proton mass and  $\nu_0$  is the central Ly $\alpha$  frequency,  $\nu_0 = 2.47 \times 10^{15}$  Hz. In the presence of

The optical depth through a column of hydrogen,  $N_{\text{HI}}$ , for a photon in the line center,  $\tau_0$  is given by

$$\begin{aligned} \tau_0 &= N_{\text{HI}} \sigma_0 = N_{\text{HI}} f_{12} \frac{\sqrt{\pi} e^2}{m_e c \Delta\nu_D} = \\ &= 8.3 \times 10^6 \left( \frac{N_{\text{HI}}}{2 \times 10^{20} \text{ cm}^{-2}} \right) \left( \frac{T}{2 \times 10^4} \right)^{-0.5}, \end{aligned} \quad (1)$$

where  $\sigma_0$  is the Ly $\alpha$  absorption cross section in the line center,  $f_{12} = 0.4167$ , the oscillator strength and  $m_e$  and  $e$  are the mass and charge of the electron, respectively. The optical depth for a photon at frequency  $x$  is reduced to

$$\frac{\tau_x}{\tau_0} = H(a, x) = \frac{a}{\pi} \int_{-\infty}^{\infty} \frac{e^{-y^2} dy}{(y-x)^2 + a^2} = \begin{cases} \sim e^{-x^2} & \text{core;} \\ \sim \frac{a}{\sqrt{\pi} x^2} & \text{wing,} \end{cases} \quad (2)$$

where  $a$  is the Voigt parameter and is the ratio of the Doppler to natural line width, given by  $a = A_{21}/4\pi\Delta\nu_D = 4.7 \times 10^{-4}$  ( $13 \text{ km s}^{-1}/v_{th}$ ), where  $A_{21}$  is the Einstein A-coefficient for the transition. The transition between 'wing' and 'core' occurs at  $x \sim 2.5 - 4.0$  for  $a \sim 10^{-2} - 10^{-6}$ .

When a Ly $\alpha$  photon of frequency  $x_i$  is absorbed by an atom, it re-emits a Ly $\alpha$  photon of the same frequency in its own frame, unless the atom is perturbed while in the excited  $2p$

state. These perturbations include collisions with an electron and photo-excitation or ionization by another photon. In this case, the energy of the re-emitted Ly $\alpha$  photon,  $x_o$ , is not equal to  $x_i$ . In most astrophysical conditions these perturbations can be neglected (see appendix C), rendering the scattering coherent in the frame of the atom.

Due to the atom's motion however, the scattering is not coherent in the observer's frame. A simple relation exists between the incoming and outgoing frequency,  $x_i$  and  $x_o$ , and the velocity of the atom,  $\vec{v}_a$ :

$$x_o = x_i - \frac{\vec{v}_a \cdot \vec{k}_i}{v_{th}} + \frac{\vec{v}_a \cdot \vec{k}_o}{v_{th}} + g(\vec{k}_i \cdot \vec{k}_o - 1) + \mathcal{O}\left(\left[\frac{v_{th}}{c}\right]^2\right), \quad (3)$$

where  $\vec{k}_i$  and  $\vec{k}_o$  are the propagation directions of the incoming and outgoing photons, respectively. The second to last term on the RHS is the 'recoil' term, which accounts for the transfer of a small amount of momentum from the photon to the atom during each scattering (exactly as in Compton scattering, e.g. Rybicki & Lightman 1979, p.196). The factor  $g$  is the average fractional amount of energy transferred per scattering. Field (1959) showed that  $g$  can be written as  $g = h\Delta\nu_D/2kT = 2.6 \times 10^{-4}$  ( $13 \text{ km s}^{-1}/v_{th}$ ). The effect of recoil is (and has been verified to be) negligible in the applications presented in this paper (see Adams 1971, for more details).

Because  $x_i$  and  $x_o$  are related via eq. (3) this case is referred to as 'partially coherent'. The redistribution function,  $q(x_o, x_i)dx_o$ , gives the probability that a photon that was absorbed at frequency  $x_i$  is re-emitted in the frequency range  $x_o \pm dx_o/2$  (in the observer's frame). Under the assumption that the velocity distribution of atoms is (locally) Maxwellian, Unno (1952) and Hummer (1962) calculated the redistribution function analytically for partially coherent scattering (historically written as  $q_H(x_o, x_i)$ ). Their calculation provides a good test case for our code, which is discussed in Appendix A.

Photons in the core have a short mean free path, and the rate at which they are scattered is high. The majority of these scattering events leave the photon in the core, but a chance encounter with a rapidly moving atom may move it to the wing, where its mean free path is much larger. In moderately optically thick media,  $\tau_0 \lesssim 10^5$ , one such encounter may be enough to enable the photon to escape in a single flight. Adams (1972) demonstrated that in the case of extremely optically thick media,  $\tau_0 \gtrsim 10^3/a$ , photons do not escape in a single flight, but rather in a single 'excursion'. During this excursion the photon scatters multiple times in the wing, and diffuses through real and frequency space. Because of the significantly increased mean free path, a photon predominantly diffuses spatially, while it is in the wing. Each scattering in the wing pushes the photon back towards the core by an average amount of  $-1/x$  (Osterbrock 1962).

The transfer of Ly $\alpha$  photons through a static, uniform, non-absorbing, plane-parallel scattering medium (hereafter referred to as "slab") has been studied extensively (e.g. Adams 1972; Harrington 1973; Neufeld 1990). The spectrum of Ly $\alpha$  photons emerging from both moderately and extremely optically thick slabs is double peaked and, when bulk motions in the gas are absent and when recoil is ignored, symmetric around the origin. The spectra of Ly $\alpha$  photons emerging from extremely optically thick slabs have been calculated analytically by Harrington (1973) and Neufeld (1990). For example, when photons are injected in the center of the slab, in the line center, the location of the peaks at  $\pm x_p$  is given by  $x_p = 1.06(a\tau_0)^{1/3}$  (Har-

rington 1973; Neufeld 1990), in which  $\tau_0$  is the total line center optical depth from the center to the edge of the slab<sup>1</sup>.

### 3. THE CODE AND TESTS

#### 3.1. The Code

Our Monte Carlo computations are based on the method presented by ZM02. Our code focuses on spherically symmetric gas configurations. We use  $N_{\text{grid}}$  spherical shells, each with their own radius, density, neutral fraction of hydrogen and velocity. The temperature is assumed to be the same in each shell, although the code can easily be adjusted to account for temperature variations. Throughout this paper, we used  $N_{\text{grid}} = 1000$ . Tests performed with 10 times more shells produced identical results. Runs performed with  $\sim 10$  times less shells still produced visually indistinguishable results. Because runs with  $N_{\text{grid}} = 100$  barely reduced the computing time,  $N_{\text{grid}} = 1000$  was used. The shells were spaced such that every shell contains roughly an equal column of hydrogen from its inner to its outer radius.

The creation and transfer of individual Ly $\alpha$  photons is described below. In the transfer problem, we identify three relevant frames: the 'central observer' frame; the frame of the shell through which the photon is traveling; and the frame of the atom that scatters the Ly $\alpha$  photon (note that the frame of the atom differs from that of the shell it is in, because of the thermal motion of the atom). The 'central observer' frame is the frame of an observer located in the center of the sphere. The reason that the observer is put in the center is that it fully exploits spherical symmetry. The bulk motion of the gas is simply pointed toward (for infall) or away (for outflows) from the observer. Photons propagating outwards and inwards, propagate away and towards the observer, respectively. From now on the 'central observer' frame will be referred to simply as the observer's frame.

A quantity ' $Q$ ' measured in the frame of a shell, observer and the atom is denoted by  $Q'$ ,  $Q$  and  $\bar{Q}$ , respectively.  $R_n$ , with  $n = 1, 2, 3, \dots$ , are random numbers generated between 0 and 1, whereas  $C_n$  and  $S_n$ , with  $n = 1, 2, 3, \dots$ , are  $\cos 2\pi R_n$  and  $\sin 2\pi R_n$ , respectively.

*Step 1.* Given the emissivity per unit volume as a function of radius,  $j(r)$ , we generate the radius of emission  $r_{em}$  from the probability distribution function:

$$R_1 = \frac{\int_0^{r_{em}} r'^2 j(r') dr'}{\int_0^{r_{max}} r'^2 j(r') dr'}, \quad (4)$$

where  $r_{max}$  is the radius of the gas sphere's edge. The location of the photon in the sphere,  $\vec{r} \equiv (p_x, p_y, p_z)$ , is given by  $(p_x, p_y, p_z) = r_{em} (S_2 C_3, S_2 S_3, C_2)$ . The emissivity  $j(r)$  depends on what model we consider, which is discussed in § 5.2.

*Step 2.* Given the location of emission, we generate the direction of emission  $\vec{k}_i = (k_x, k_y, k_z) = (R_4 C_5, R_4 S_5, (1 - R_4^2)^{0.5})$ . In the case the gas has a bulk velocity, the frequency of the emitted photon is given by  $x_i = x'_i + \vec{k}_i \cdot \vec{v}_{\text{bulk}}/v_{th}$ , where  $\vec{v}_{\text{bulk}}$  is the bulk velocity vector of the gas at the location of emission. For

<sup>1</sup>Note that the value of  $x_p$  quoted by Harrington (1973); Neufeld (1990), is actually  $x_p = 0.88(a\tau_0)^{1/3}$ . This is due to their different definition of  $H(a, x)$ , which is lower by a factor of  $\sqrt{\pi}$  (their  $H(a, x)$  is normalized to 1, whereas ours has  $H(a, 0) = 1$ ). To obtain the same physical optical depth for a given column of hydrogen,  $\tau_x = \tau_0 H(a, x)$ , their value of  $\tau_0$  is  $\sqrt{\pi}$  higher (see Ahn et al. 2002).

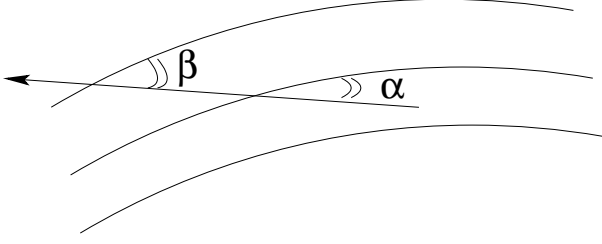


FIG. 1.— A photon propagating in direction  $\vec{k}$  intersects each spherical shell under a different angle. Here,  $\alpha \neq \beta$ .

simplicity, we set  $x'_i = 0$ , which means that the Ly $\alpha$  is initially always injected at the line center in the frame of the gas shell in which it is emitted. In reality  $x'_i$  is distributed according to the Voigt profile (eq. 2). This minor simplification does not affect our results at all. The reason is that the Ly $\alpha$  photon is redistributed in frequency each time it is scattered, rapidly erasing any ‘memory’ of its initial frequency. For our spherically symmetric models,  $\vec{v}_{\text{bulk}} = v_{\text{bulk}} \vec{r}/|\vec{r}|$ , where  $v_{\text{bulk}}$  is the infall/outflow speed of the gas at radius  $r$ . The sign of  $v_{\text{bulk}}$  is negative/positive for infall/outflow, respectively.

*Step 3.* The optical depth  $\tau$  the photon is allowed to travel is given by  $-\ln[R_6]$ . To convert  $\tau$  to a physical distance, we calculate the physical distance  $d_e$  to the edge of the shell in which the photon is emitted in the direction  $\vec{k}_i$ . The corresponding optical depth to the edge of the shell is  $\tau_e = d_e n_H \sigma_0 \phi(x'_i)$ , where  $n_H$  is the number density of neutral hydrogen atoms in the shell. If  $\tau_e > \tau$ , then the new location is given by  $\vec{r} + \lambda \vec{k}_i$ , where  $\lambda = d_e \tau / \tau_e$ . If  $\tau_e < \tau$  then, we obtain the frequency of the photon in the frame of the next shell from  $x'_i = x_i - \vec{k}_i \cdot \vec{v}_{\text{bulk}} / v_{\text{th}}$ , where  $\vec{v}_{\text{bulk}}$  is now the bulk velocity vector of the gas where the photon penetrates the next shell. As illustrated schematically in Figure 1, the angle under which the photon enters a new shell is generally (slightly) different for each shell. In the next shell  $\tau$  is replaced by  $\tau - \tau_e$ . This process is repeated until the photon has traveled the generated optical depth  $\tau$  to its new position  $\vec{r}$ .

*Step 4.* When  $|\vec{r}| > r_{\text{max}}$ , the photon’s frequency and the angle under which it passed through the surface of the sphere are recorded. Otherwise, the photon is scattered by a hydrogen atom, in which case we proceed to the next step.

*Step 5.* Once the location of scattering,  $\vec{r}$ , has been determined, the total velocity of the atom,  $\vec{v}_a$ , that scatters the Ly $\alpha$  photon is generated. The total velocity is given by the sum of the bulk velocity of the gas plus the thermal velocity:  $\vec{v}_a = \vec{v}_{\text{bulk}} + \vec{v}_{\text{th}}$ . The thermal velocity of the atom doing the scattering,  $\vec{v}_{\text{th}}$ , is decomposed into two parts. Following ZM02, the magnitude of the atom’s velocity in the direction  $\vec{k}_i$ ,  $u_{\parallel}$ , is generated from eq. (5),

$$u_{\parallel} = \frac{a}{\pi H(a, x'_i)} \int_{-\infty}^{R_9} \frac{e^{-y^2}}{(x'_i - y)^2 + a^2} dy. \quad (5)$$

This distribution reflects the strong preference for photons at frequency  $x'_i$ , to be scattered by atoms to which they appear exactly at resonance,  $u_{\parallel} = x'_i$ . For large  $x'_i$ , however, the number of these atoms reduces as  $\propto e^{-x'^2_i}$  and the photon is likely scattered by an atom to which it appears far in the wing.

The two (mutually orthogonal) components perpendicular to  $\vec{k}_i$ ,  $u_{\perp 1,2}$ , are drawn from a Gaussian distribution with zero mean and standard deviation  $2^{-1/2} v_{\text{th}}$  (the velocity dispersion of the

gas). Following the procedure described in Numerical Recipes (Press et al. 1992):

$$\begin{aligned} u_{\perp 1} &= \sqrt{-\ln[R_{11}]} \cos(2\pi R_{10}) \\ u_{\perp 2} &= \sqrt{-\ln[R_{11}]} \sin(2\pi R_{10}), \end{aligned} \quad (6)$$

where  $u_{\perp 1,2}$  is in units of  $v_{\text{th}}$ . At this particular step in the code, it is possible to speed up the code significantly, which is described below (§3.1.1).

*Step 6.* In the frame of the atom, the distribution of the direction of the re-emitted photon with respect to that of the incoming photon is given by a dipole distribution,

$$R_7 = \frac{3}{8} \int_{-1}^{\mu} (1 + \mu'^2) d\mu', \quad (7)$$

where  $\mu \equiv \vec{k}_i \cdot \vec{k}_o$ . Given  $\vec{k}_i$ , we have  $\vec{k}_o = \mu \vec{k}_i + (1 - \mu^2) \vec{k}_{\perp}$ , where  $\vec{k}_{\perp}$  is an arbitrary unit vector perpendicular to  $\vec{k}_i$ .  $\vec{k}_o$  is calculated from  $\vec{k}_o$  via a Lorentz transformation into the observer’s frame. Once  $\vec{v}_a$  and  $\vec{k}_o$  are known,  $x_o$  can be calculated using eq. 3. After replacing  $x_i$  and  $\vec{k}_i$  by  $x_o$  and  $\vec{k}_o$ , respectively, we return to step 3.

### 3.1.1. Accelerated Scheme

It is possible to speed up the code using a method described by Ahn et al. (2002). We introduce a critical frequency  $x_{\text{crit}}$ , which defines a transition from ‘core’ to ‘wing’. Once a photon is in the core ( $|x'| < x_{\text{crit}}$ ), it is possible to force it (back) into the wing, by only allowing the photon to scatter off a rapidly moving atom. This can be achieved when generating  $u_{\perp 1,2}$  (under Step 5. in §3.1). Instead of drawing them from a Gaussian distribution, a truncated Gaussian distribution is used, which is Gaussian for  $u > x_{\text{crit}}$ , but 0 for  $u < x_{\text{crit}}$ . To be more precise:

$$\begin{aligned} u_{\perp 1} &= \sqrt{x_{\text{crit}}^2 - \ln[R_{11}]} \cos(2\pi R_{10}) \\ u_{\perp 2} &= \sqrt{x_{\text{crit}}^2 - \ln[R_{11}]} \sin(2\pi R_{10}), \end{aligned} \quad (8)$$

where  $u_{\perp 1,2}$  is again in units of  $v_{\text{th}}$ .

The main reason that it is allowed to skip core scattering is that spatial diffusion occurs predominantly in the wings (see § 2). Skipping scatterings in the core, basically sets the mean free path in the core to 0. Clearly,  $x_{\text{crit}} = 0$  restores the non-accelerated version of the code. Unless stated otherwise, in this paper we used  $x_{\text{crit}} = 3$ . We found that larger values of  $x_{\text{crit}}$  changed the appearance of the spectrum, especially the presence of the red peak (see below) was strongly affected.

### 3.2. The Tests

We performed various tests on the code, three of which are described in Appendix A. The other test is explicitly described here, since it involves a new analytic solution we derived in Appendix B. The test is similar to one generally done by other groups (e.g. Ahn et al. 2000, 2002; Cantalupo et al. 2005, ZM02), but differs in the geometry of the gas distribution. Ly $\alpha$  photons are injected at  $x = 0$  in the center of a uniform non-absorbing sphere with the gas at  $T = 10^4 \text{ K}$ , which corresponds to  $a = 1.5 \times 10^{-2}$ . The line center optical depth from the center to the edge of the sphere is  $\tau_0$ . In the upper left panel of Figure 2 the emergent spectra are shown for three different values of  $\tau_0$ :  $\tau_0 = 10^5, 10^6$  and  $10^7$  and compared to the analytic solution given below.

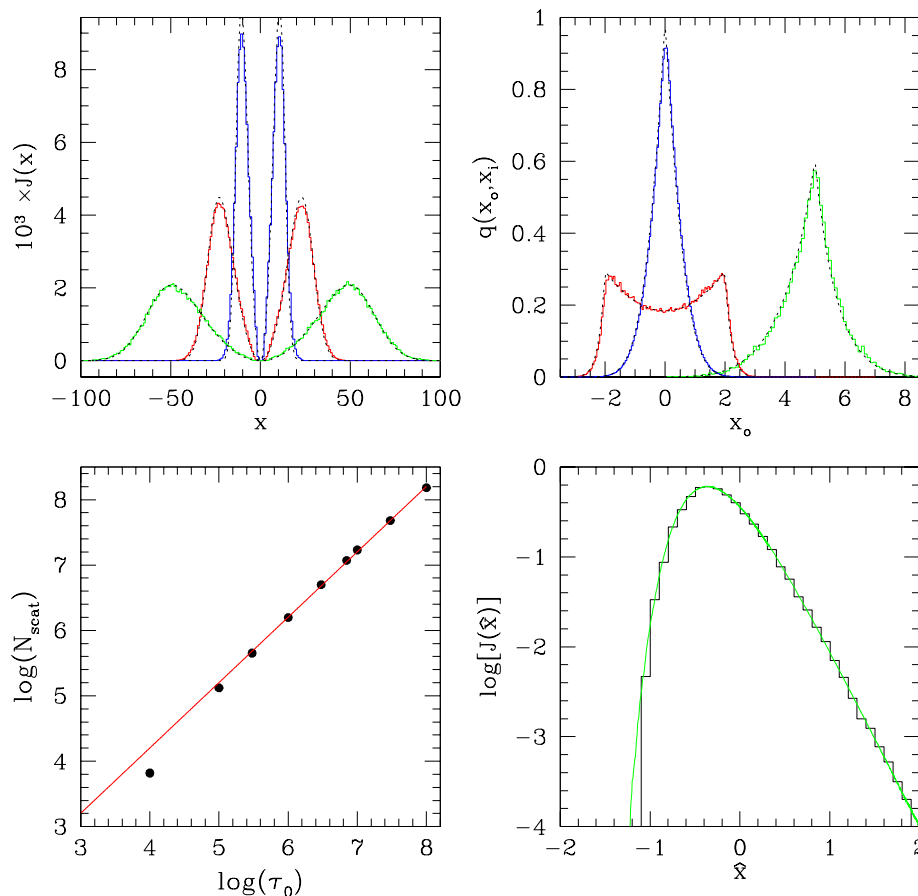


FIG. 2.— The panels in this figure show four different tests of our Monte Carlo code against known analytic solutions and Monte Carlo calculations by Loeb & Rybicki (1999). *Upper left panel:* The spectrum emerging from a uniform spherical gas cloud, in which Ly $\alpha$  photons are injected in the line center,  $x = 0$ . The total line center optical depth,  $\tau_0$  from the center to the edge is  $10^5$  and  $10^7$  for the narrowest (blue) and broadest (green) profile, respectively. The intermediate spectrum (red) corresponds to  $\tau_0 = 10^6$ . Overplotted as the black dotted line is the theoretically derived spectrum, eq. (9). The tests that are shown in the other panels are described in Appendix A. *Upper right panel:* The colored histograms are the redistribution functions,  $q_{II}(x', x)$ , for  $x = 0$  (blue),  $x = 2$  (red) and  $x = 5$  (green), as extracted from the code. The solid lines are the analytic solutions given in Hummer (1962) and Lee (1974). *Lower left panel:* The total number of scatterings a Ly $\alpha$  photon undergoes before it escapes from a slab of optical thickness  $2\tau_0$  as extracted from the code (filled circles). Overplotted as the red–solid line is the theoretical prediction by Harrington (1973). *Lower right panel:* The spectrum emerging from an infinitely large object that undergoes Hubble expansion. The histogram is the output from our code, while the green–solid line is the (slightly modified) solution obtained by Loeb & Rybicki (1999) using their Monte Carlo algorithm.

$$J(x) = \frac{\sqrt{\pi}}{\sqrt{24}a\tau_0} \left( \frac{x^2}{1 + \cosh \left[ \sqrt{\frac{2\pi^3}{27}} \frac{|x^3|}{a\tau_0} \right]} \right) \quad (9)$$

The derivation of this analytic solution for a sphere is completely analogous to the derivation given by Harrington (1973) and Neufeld (1990), and can be found in Appendix B. As mentioned in § 2, the emergent spectra are double-peaked and symmetric around the origin, with  $x_p$  increasing with  $\tau_0$ . For a given value of  $\tau_0$ ,  $x_p = 0.92(a\tau_0)^{1/3}$  (vs.  $x_p = 1.06(a\tau_0)^{1/3}$  for a slab). The spectra are normalized (as is the analytic solution) such that the area under all curves is  $(2\pi)^{-1}$ . The figure shows that the agreement is good. In Appendix A other tests are performed on the code that involve core scattering and a case in which the gas has bulk motions. Here, we briefly summarize these tests: In the *upper right panel* the redistribution functions,  $q_{II}(x', x)$ , for  $x = 0$  (blue),  $x = 2$  (red) and  $x = 5$  (green), as extracted from the code are compared with the analytic solutions given in Hummer (1962) and Lee (1974) (solid lines). The total number of

scatterings a Ly $\alpha$  photon undergoes before it escapes from a slab of optical thickness  $2\tau_0$  as extracted from the code (filled circles) is shown in the *lower left panel*. Overplotted as the red–solid line is the theoretical prediction by Harrington (1973). In the *lower right panel* we show the spectrum emerging from an infinitely large object that undergoes Hubble expansion. The histogram is the output from our code, while the green–solid line is the (slightly modified) solution obtained by Loeb & Rybicki (1999, hereafter LR99) using their Monte Carlo code. As Figure 2 shows, the code passes all these tests well.

#### 4. DEUTERIUM

Although it has a low abundance, accounting for deuterium may be relevant when predicting spectra emerging from Ly $\alpha$  emitters. The resonance frequency of the deuterium Ly $\alpha$  absorption line is blueshifted by 82 km s $^{-1}$  with respect to that of hydrogen. For a gas at  $T \equiv T_4 \times 10^4$  K, this corresponds to  $x_D \equiv +6.3 (T_4)^{-1/2}$ . According to eq. (2), the hydrogen optical depth at this frequency is reduced to  $\tau_{x_D, H} \sim 6.6 \times 10^{-6} T_4^{1/2} \tau_0$ .

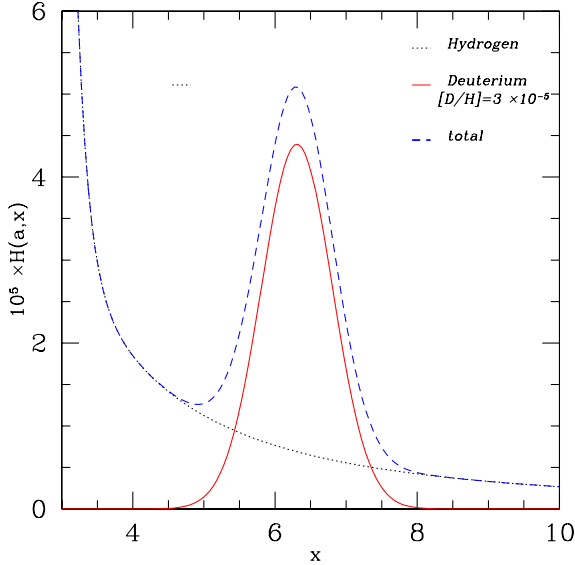


FIG. 3.— This figure shows the potential importance of deuterium for  $\text{Ly}\alpha$  transfer. The ratio of the optical depth at frequency  $x$  and frequency  $x=0$ ,  $\tau_{x,H}/\tau_0 \equiv H(a,x)$ , through static gas is shown. The *black-dotted line* is for hydrogen only (and is given by eq. 2); the *red-solid line* is for deuterium only; the *blue-dashed line* is their sum. The deuterium abundance is assumed to be  $[D/H] = 3 \times 10^{-5}$ . In the range  $x = 5-8$ , deuterium dominates the opacity.

At this frequency, the photon is (by definition) exactly in the deuterium line center, and the optical depth due to deuterium is  $\tau_{x,D} = 2^{1/2}[D/H]\tau_0 \sim 4.4 \times 10^{-5}\tau_0$ , where  $[D/H]$  is the number of deuterium atoms per hydrogen atom,  $[D/H] = 3 \times 10^{-5}$  (Burles & Tytler 1998). The factor  $2^{1/2}$  reflects that deuterium is two times heavier than hydrogen, which reduces its thermal velocity by  $2^{1/2}$ , which according to eq. (1) increases the line center optical depth by  $2^{1/2}$ . Additionally, the reduced thermal velocity of deuterium raises its Voigt parameter by  $2^{1/2}$ . The contribution of deuterium to the optical depth,  $\tau_{x,D}/\tau_0$ , is shown as a function of frequency in the range  $x = 3-10$  (*red-solid line* in Figure 3). The *black-dotted line* shows the original  $\tau_{x,H}/\tau_0$  given by eq. (2). The (*blue-dashed line*) shows the sum of the two. The gas is assumed to be at  $10^4 \text{ }^\circ\text{K}$ . Clearly there is a range in frequencies,  $x \sim 5-8$ , where deuterium dominates the optical depth and regulates the transfer of  $\text{Ly}\alpha$  photons. Despite extensive research on  $\text{Ly}\alpha$  radiative transfer, this detail has been neglected, to our knowledge, in all previous studies.

To include deuterium in our code we added the contribution of deuterium,  $\tau_{x,D}$ , to  $\tau_x$ . In addition to this, a step was added to the code following *Step 4*. (§ 3.1), that determines whether a scattering occurs by a hydrogen or deuterium atom. A random number  $R_D$  was generated between 0 and 1. Let  $P_H \equiv \tau_{x,H}/[\tau_{x,H} + \tau_{x,D}]$ , be the probability that the  $\text{Ly}\alpha$  photon is scattered by hydrogen. When  $R_D \leq P_H$ , the scattering is done by hydrogen, in which we proceed as described under *Step 5*. in §3.1. Otherwise, the scattering is done by deuterium and its velocity vector is generated in exactly the same way, but with  $a$  and  $x$  replaced by  $2^{1/2}a$  and  $2^{1/2}[x - 82 \text{ km s}^{-1}/v_{th}]$ , respectively.

Figure 4 demonstrates the impact of deuterium on the  $\text{Ly}\alpha$  spectrum emerging from a uniform sphere in which the photons are injected at line center ( $x = 0$ ) in the sphere's center. The gas is at  $T = 10^4 \text{ }^\circ\text{K}$  and the total column of hydrogen

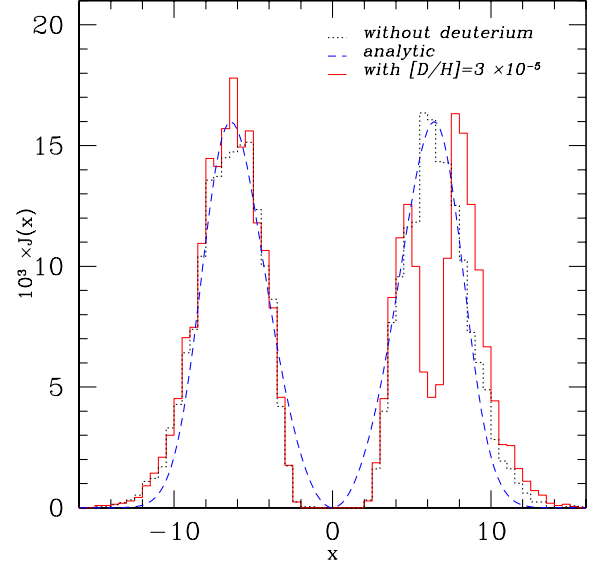


FIG. 4.— The effect of deuterium on the spectrum emerging from a sphere with a center-to-edge column density of hydrogen of  $N_{\text{HI}} = 1.2 \times 10^{19} \text{ cm}^{-2}$ . The deuterium abundance is assumed to be  $[D/H] = 3 \times 10^{-5}$ . The reduced mean free path of photons in the frequency range inhibits their escape, which modifies the spectrum.

from the center to the edge of the sphere is  $N_{\text{HI}} = 1.2 \times 10^{19} \text{ cm}^{-2}$ , yielding  $\tau_0 = 7.3 \times 10^5$  (eq. 1). The emerging spectrum is shown with (*red-solid-histogram*) and without (*black-dotted-histogram*) deuterium taken into account. The *blue-dashed line* is the theoretically predicted spectrum, eq (9). The reason the theoretical curve does not fit very well is that the product  $a\tau_0 = 343$ , while Neufeld (1990) requires  $a\tau_0$  to be  $a\tau_0 \gtrsim 10^3$  for the theoretical curve to provide a good fit. The imprint deuterium leaves on the spectrum is strong. The main reason is that the presence of deuterium reduces the mean free path for photons near  $x = x_D$ , which reduces the probability that they escape the medium at this frequency. We find that even for a 10 times lower deuterium abundance, the imprint in the spectrum is still noticeable.

For deuterium to leave an observable imprint in the spectrum, the range of frequencies it affects, should roughly correspond to the frequencies at which a non-negligible fraction of the  $\text{Ly}\alpha$  photons eventually emerge (as in Fig. 4). For  $T_4 = 1$ , for example, we expect deuterium to leave a spectral feature for columns in the range  $N_{\text{HI}} = 10^{18} - 10^{20} \text{ cm}^{-2}$ , since this range would translate to  $x_p \sim (a\tau_0)^{1/3} \sim 3-12$ . It is interesting that this corresponds to the range of column densities in Lyman limit systems. Because the columns studied in this paper are much larger, typically  $10^{21} - 10^{22} \text{ cm}^{-2}$ , only a small fraction of the photons emerge from the object at the frequencies at which deuterium regulates the  $\text{Ly}\alpha$  transfer and the spectral feature due to deuterium is much less prominent. Furthermore, bulk motions in the gas will most likely smear the absorption feature over a wide frequency range, which makes it even harder to observe in practise. A further challenge is that the frequency range of the deuterium feature corresponds to 3 thermal widths, or  $v \sim 40 \text{ km s}^{-1}$ . To resolve this narrow feature, spectra are required with  $R \sim 20000$ . This resolution can be achieved with the High Resolution Echelle Spectrometer (HIRES) on *Keck*. Its detectability depends, however, on the brightness of  $\text{Ly}\alpha$  emission. The brightest known  $\text{Ly}\alpha$  blobs are  $\sim 10^{-15} \text{ ergs s}^{-1} \text{ cm}^{-2}$  (Steidel

et al. 2000), which corresponds to  $m_{AB} \sim 20.7$ , which is fainter by  $\sim 3-4$  magnitudes than the sources successfully observed with this instrument. We plan to address the feasibility of detecting deuterium in more detail in future work.

## 5. LY $\alpha$ EMISSION FROM NEUTRAL COLLAPSING GAS CLOUDS

### 5.1. Physics of Cloud Collapse and Ly $\alpha$ Generation

For gas to collapse inside its host dark matter halo, it must lose its gravitational binding energy. In the standard picture the kinetic energy of infalling gas is converted to thermal energy when the gas reaches the virial radius, where it is shocked to the virial temperature of the dark matter halo,  $T_{vir}$ . When the cooling time is less than the dynamical time, the gas is practically in the same configuration by the time it has cooled down to  $10^4$  °K. Since this gas is no longer pressure supported, it falls inward on a dynamical timescale (Rees & Ostriker 1977). Haiman et al. (2000) argued that a large fraction of the gravitational binding energy is emitted in the Ly $\alpha$  line. Birnboim & Dekel (2003) presented a refined version of the previous scenario, and used analytical arguments in combination with a 1-D hydro simulation to show that virial shocks do not exist in halos with  $M \lesssim 2 \times 10^{11} M_\odot$  (which at  $z = 3$  translates to  $v_{circ} \lesssim 130$  km s $^{-1}$ ). Consequently, the gas in these halos never gets shocked to the virial temperature and the gas is accreted ‘cold’ (also see Thoul & Weinberg 1995). Fardal et al. (2001) and Keres et al. (2004) found, using 3-D smoothed particle hydrodynamics (SPH), their result to be a combination of the two described above.

The main purpose of this section is to demonstrate that the physical picture associated with the accretion of cold gas is not clear. Birnboim & Dekel (2003) sketch a scenario in which the gas freely plunges into the center, where its kinetic energy is converted to heat, which is radiated away in soft X-Rays. As a result, an HII region forms in which photo-ionization and subsequent recombination, converts  $\sim 68\%$  of the ionizing radiation into Ly $\alpha$ . The radius of this HII region is set by the details of the gas distribution in the center and by the mean energy of the ionizing photons. To contrast this scenario with the one sketched below, we assume that the HII region will be small, causing the Ly $\alpha$  emissivity to be strongly concentrated.

Haiman et al. (2000) describe an alternative scenario that is inspired by 3-D simulations, that show that any halo is build up of mergers of pre-existing clumps. This clumpy gas distribution fits in well with models of multiphase galaxy formation (Fall & Rees 1985; Maller & Bullock 2004), in which thermal instabilities in the gas cause cool clumps to condense out of the hot,  $T \sim T_{vir}$ , ambient gas phase, with both phases in pressure equilibrium. Haiman et al. (2000) sketch a scenario in which the denser cold clumps fall inwards, while experiencing weak secondary shocks from supersonic encounters with other density inhomogeneities. As a result, the clumps are continuously heated, which is balanced by cooling through Ly $\alpha$  emission. In the most extreme case of their scenario, the clumps fall in at a constant speed and all the gravitational binding energy of a clump is converted into heat which is radiated away in the Ly $\alpha$  line. The Ly $\alpha$  emissivity associated with this scenario is spatially extended.

The main difference between the two scenarios of how gas cools and collapses, sketched above, is the Ly $\alpha$  emissivity as a function of radius,  $j(r)$ . In the first scenario  $j(r)$  is strongly centrally concentrated, whereas in the second case Ly $\alpha$  is contin-

uously emitted at all radii. These two scenarios can be viewed as the two most extreme cases which bracket the range of astrophysically plausible models. Clearly, sub-clumping and the multiphase nature of galaxy formation are not captured by our spherically symmetric simulation. It is possible, however, to calculate the effect  $j(r)$  has on observable quantities like the spectrum and surface brightness distribution, which will be done below.

### 5.2. Modeling the Gas Kinematics and Ly $\alpha$ Emissivity Profile

As mentioned above, the emissivity,  $j(r)$ , is one of the main model uncertainties. The main purpose of this section is to discuss *all* model parameters and their uncertainties. Input that is kept fixed in all models is the density distribution of the dark matter,  $\rho_D(r)$ , which is given by a NFW profile with concentration parameter  $c = 5$ . Also, the gas temperature is assumed to be  $10^4$  K for all models. As discussed in § 8, changing the gas temperature, does not affect our main results. The density distribution of the baryons,  $\rho_b(r)$ , is assumed to trace the dark matter at large radii, with a thermal core at  $r < 3R_s/4$  (see Maller & Bullock 2004, their eq. 9-11, where  $R_s = R_{vir}/c$ ). Although the results are not presented in this paper, we found the effect of varying the concentration parameter  $c$  to have no significant impact on our results. Input that is varied can be put into two categories. The *first category* contains input that is varied to cover a range of parameter space that is known to exist in the universe. These parameters include,

- $M_{tot}$ , the total (dark matter + baryons) mass of the system. The mass range covered in this paper is  $10^{10} - 10^{13} M_\odot$ . Related quantities are the circular velocity,  $v_{circ}$ , and virial temperature,  $T_{vir}$ . The upper limit on this mass range is set by simple cooling arguments: the cooling time of objects exceeding  $10^{13} M_\odot$  exceeds the Hubble time (e.g Blumenthal et al. 1984). The lower limit corresponds to the mass that is not affected by the UV background ( $10^{10} M_\odot$  corresponds to  $v_{circ} \sim 50$  km s $^{-1}$  at  $z = 3$ , see e.g. Thoul & Weinberg 1996; Dijkstra et al. 2004).
- The redshift  $z_{vir}$  at which the system virializes. The redshift range covered in this paper is  $z_{vir} = 3-6$ . The lower limit is set by the redshift of the observed Ly $\alpha$  blobs which are candidates for cooling radiation. The upper limit is set by the opacity of the IGM which, as we will discuss below, drastically increases beyond  $z \gtrsim 6$ .

The *second category* contains input that reflects our ignorance of the Ly $\alpha$  emissivity and of the dynamics of the protogalactic gas, through which the photons are propagating. This input includes:

- The velocity field,  $v_{bulk}(r)$ , is given by a simple power law  $v_{bulk}(r) = v_{amp}[r/r_{vir}]^\alpha$ . A spherical top-hat model would have  $\alpha = 1$  and  $v_{amp} = v_{circ}$ . This can be seen by time-reversing solutions for trajectories initially following Hubble expansion,  $v \propto r$ . In more realistic initial density profiles (e.g. Bertschinger 1985), the mean density within radius  $r$  decreases smoothly with radius, causing the inner shells to be decelerated more relative to the overall expansion of the universe. This enhances the infall speed at small  $r$  relative to that in the top-hat model. The result of this is a flatter velocity profile, i.e

$\alpha < 1$ . A lower limit on  $\alpha$  is set by accretion of massless shells onto a point mass in which  $\alpha = -1/2$ . We therefore study values of  $\alpha$  in the range  $\alpha \in [-0.5, 1]$ . For cases with  $\alpha < 0$ , the velocity diverges as  $r \rightarrow 0$ . This artificially boosts the emission at small  $r$ . To prevent this, these cases are modified to flatten at  $r \lesssim r_v$ :

$$v_{\text{bulk}}(r) = v_{\text{amp}} \left[ \frac{r_v + r}{r_v + r_{\text{vir}}} \right]^\alpha. \quad (10)$$

When  $r \gg r_v$ ,  $v_{\text{bulk}} = v_{\text{amp}}[r/r_{\text{vir}}]^\alpha$  and when  $r \rightarrow 0$ , then  $v_{\text{bulk}} \rightarrow v_{\text{max}}$ . We set  $v_{\text{max}} = 2v_{\text{amp}}$ , which uniquely determines  $r_v$ . The amplitude of the velocity field  $v_{\text{amp}}$  is also varied between 0 and  $2 v_{\text{circ}}$ .

- The emissivity,  $j(r)$ , which we take to be either ‘continuous’ or ‘central’. The continuous case refers to the scenario sketched by Haiman et al. (2000), in which the gas continuously emits a fraction  $f_\alpha$  of the change of its gravitational binding energy in the Ly $\alpha$  line. The emissivity as a function of radius  $j(r)$ , in ergs  $\text{s}^{-1} \text{cm}^{-3}$ , is then given by

$$j(r) = f_\alpha \frac{G M_{\text{tot}}(< r) \rho_b}{r^2} \frac{dr}{dt}, \quad (11)$$

where  $M_{\text{tot}}(< r)$  is the total mass enclosed within radius  $r$ ,  $\rho_b$  the mass density of baryons at radius  $r$  and  $dr/dt$  is simply  $v_{\text{bulk}}$ , the speed at which the gas at radius  $r$  is falling in. We assume  $f_\alpha=1$ , which reflects extreme cases in which all gravitational binding energy is converted into Ly $\alpha$ . The results given below scale linearly with  $f_\alpha$ .

The ‘central’,  $j(r) = \mathcal{K}\delta(r)$ , models represent the extreme version of the scenario sketched by Birnboim & Dekel (2003), in which all Ly $\alpha$  is only generated in the center. These central models may represent any model in which a central Ly $\alpha$  emitting source is surrounded by a neutral collapsing gas cloud. We determine  $\mathcal{K}$  from we the total Ly $\alpha$  luminosity, given by  $L_{\text{Ly}\alpha} \equiv \int dV j(r)$ . For two models that differ only in their  $j(r)$ , we set  $L_{\text{Ly}\alpha}$  for the central model to be equal to that of the continuous model, although it is likely to be different.

A brief summary of all models studied in this paper is given in Table 1. For each model, its associated set of model parameters  $M_{\text{tot}}$ ,  $z_{\text{vir}}$ ,  $\alpha$  and  $v_{\text{amp}}$  is given. To get a sense of the physical infall velocities of the gas, the circular velocity for each model is given. The first and last column contains the model number of the model in which the emissivity was ‘continuous’ and ‘central’, respectively (see the discussion above).

### 5.3. The IGM Transmission

The last model ingredient is related to Ly $\alpha$  transfer through the IGM, which is defined to lie beyond the virial radius. Even though the IGM is fully ionized at most redshifts considered in this paper, a small residual neutral fraction is enough to scatter some fraction of the Ly $\alpha$  photons from our line of sight. For an IGM that is comoving with the Hubble flow, the mean transmission is 1 and  $\langle e^{-\tau} \rangle$  redward and blueward of the line center, respectively (e.g. Madau 1995). Note that  $\langle e^{-\tau} \rangle$  is a function of wavelength, but over the narrow range of frequencies that the Ly $\alpha$  emerges,  $\langle e^{-\tau} \rangle$  is to a good approximation constant. The

TABLE 1  
MODELS STUDIED

Model # (Cont.)	Model # (Central)	$M_{\text{tot}}$ $10^{11} M_\odot$	$z_{\text{vir}}$	$v_{\text{circ}}$ $\text{km s}^{-1}$	$v_{\text{amp}}$ $v_{\text{circ}}$	$\alpha$
1	3	5.2	3.0	181	1.0	1.0
2	4	5.2	3.0	181	1.0	-0.5
20	60	5.2	3.8	198	1.0	1.0
21	61	5.2	4.5	212	1.0	1.0
22	62	5.2	5.2	225	1.0	1.0
23	63	5.2	6.0	240	1.0	1.0
40	75	0.1	3.0	49	1.0	-0.5
41	74	0.1	3.0	49	1.0	0.25
42	73	0.1	3.0	49	1.0	1.0
43	70	40	3.0	355	1.0	1.0
44	71	40	3.0	355	1.0	0.25
45	72	40	3.0	355	1.0	-0.5
57	55/52	5.2	3.0	181	1.0	0.25
13	51	5.2	3.0	181	0.50	1.0
14	59	5.2	3.0	181	0.25	1.0
99	58	5.2	3.0	181	$10^{-6}$	1.0
92	12	5.2	3.0	181	2.0	1.0
91	11	5.2	3.0	181	1.3	1.0

exact value of  $\langle e^{-\tau} \rangle$  is a function of redshift and is well known from studies of the Ly $\alpha$  forest (e.g. Songaila & Cowie 2002; Lidz et al. 2002; McDonald et al. 2001) and is tabulated in Table 2.

TABLE 2  
TRANSMISSION OF IGM

$z$	$2.4^1$	$3.0^1$	$3.8^1$	$4.5^2$	$5.2^2$	$5.7^2$	$6.0^2$
$f \equiv \langle e^{-\tau} \rangle$	0.8	0.68	0.49	0.25	0.09	0.07	0.004
$\sigma_f$					0.02	0.003	0.003

- (1) From McDonald et al. (2001)  
(2) From Songaila & Cowie (2002)

The naive way to incorporate the IGM in our code, is to give a photon that escaped with  $x > 0$  and  $x \leq 0$  a weight  $\langle e^{-\tau} \rangle$  and 1, respectively. However, Barkana & Loeb (2004) have recently shown that this is not correct around the massive objects considered in this paper, since their gravitational field causes material enclosed within  $\sim 10$  virial radii to decouple from the Hubble flow and move inwards (in the comoving frame Barkana 2004). As a consequence, photons that escape our object with a small redshift, can Doppler shift into resonance in this infalling IGM, and have an increased probability of being scattered out of the line of sight. The result of this is that the lower transmission can extend into the red part of the spectrum. We postpone a detailed discussion of this effect to Paper II and only quantify briefly how it changes the spectra in § 6.

## 6. RESULTS

Before discussing the spectral features and surface brightness profiles, it is useful to express the total Ly $\alpha$  luminosity,  $L_{\text{Ly}\alpha}$ , as a function of our model parameters:

$$\frac{L_{\text{Ly}\alpha}}{10^{42}} = 0.66 \left( \frac{M_{\text{tot}}}{10^{11}} \right)^{\frac{5}{3}} \left( \frac{v_{\text{amp}}}{v_{\text{circ}}} \right) \left( \frac{1+z_{\text{vir}}}{5} \right)^{\frac{5}{2}} \left( \frac{2-\alpha}{1.75} \right)^{1.2} \frac{\text{ergs}}{\text{sec}}. \quad (12)$$

The dependence of  $f_{\text{Ly}\alpha}$  on  $M_{\text{tot}}$  and  $v_{\text{amp}}$  and  $(1+z_{\text{vir}})$  is exact. The  $\alpha$  dependence is a fit, that is accurate to within 10%, over the range  $\alpha \in [-0.5, 1]$ . Note that equation (12) can be written as:

$$\frac{L_{\text{Ly}\alpha}}{10^{42}} = 0.66 \left( \frac{v_{\text{circ}}}{116 \text{ km s}^{-1}} \right)^5 \left( \frac{v_{\text{amp}}}{v_{\text{circ}}} \right) \left( \frac{2-\alpha}{1.75} \right)^{1.2} \frac{\text{ergs}}{\text{sec}}. \quad (13)$$

The dependence of  $L_{\text{Ly}\alpha}$  on  $v_{\text{circ}}$  can be understood from the following scaling relations:  $L_{\text{Ly}\alpha} \propto U/t \propto U/(R_{\text{vir}}/v_{\text{circ}}) = v_{\text{circ}}U/R_{\text{vir}} \propto v_{\text{circ}}M^2/R_{\text{vir}}^2 \propto v_{\text{circ}}^5$ , where we used that  $U \propto GM^2/R_{\text{vir}}$  and  $v_{\text{circ}}^2 = GM/R_{\text{vir}}$ .

To correctly convert this to a flux on earth is not straightforward, since the transmitted flux through the IGM is different red and blueward of the Ly $\alpha$  line center (see § 5.3), with the exact transmission near the line center strongly depending on the assumed model of the intergalactic medium (this will be shown in Paper II). We first estimate the total detectable Ly $\alpha$  flux from:  $f_{\text{Ly}\alpha} \approx \langle e^{-\tau} \rangle L_{\text{Ly}\alpha}/4\pi d_L^2$ . This estimate is motivated by the observation that the Ly $\alpha$  emerges mainly blueshifted from our models (as will be discussed in detail below). We obtain:

$$\frac{f_{\text{Ly}\alpha}}{10^{-18}} \approx 2 \left( \frac{M_{\text{tot}}}{10^{11} M_{\odot}} \right)^{\frac{5}{3}} \left( \frac{v_{\text{amp}}}{v_{\text{circ}}} \right) \left( \frac{2-\alpha}{1.75} \right)^{1.2} \times \begin{cases} \times \left( \frac{5}{1+z_{\text{vir}}} \right)^{1.75} & z \leq 4.0 \\ \times \left( \frac{5}{1+z_{\text{vir}}} \right)^{8.3} & z > 4.0 \end{cases} \frac{\text{ergs}}{\text{sec cm}^2}, \quad (14)$$

where we used  $\langle e^{-\tau} \rangle = 0.68[(1+z)/4]^{-1.5}$  for  $z \leq 4$  and  $\langle e^{-\tau} \rangle = 0.031[(1+z)/7]^{-8.1}$  for  $z > 4$ , where the last approximation was taken from (Songaila & Cowie 2002). Note that this approximation fails at  $z \geq 6$ , where the mean transmission drops even more rapidly. Furthermore, we approximated the luminosity distance by  $d_L(z) = 3.6 \times 10^4 [(1+z)/5]^{11/8}$  Mpc, which is exact to  $< 6\%$  in the range  $z = 3-10$ . For the models discussed below, we calculated the detectable flux by properly accounting for the intrinsically emitted spectrum and the frequency dependent IGM transmission. We found that the value obtained in this fashion was within a factor of  $\sim 3$  from equation (14), which is within model uncertainties. It is worth emphasizing, that for a given luminosity of cooling radiation, the total detectable flux does *not* scale with  $d_L^{-2} \propto (1+z)^{-2.75}$ . Instead the detectable flux decreases as  $\propto \langle e^{-\tau} \rangle (1+z)^{-2.75} \sim (1+z)^{-11}$  for  $z \geq 4.0$ . This conclusion does not account for the proximity effect near bright QSO's, which may allow significantly more flux to be transmitted (e.g. Cen et al. 2005).

### 6.1. Four Models of Gas Dynamics and Emissivity Profiles

Below we discuss the surface brightness profile and spectral energy distribution of four models in detail. The main purpose is to gain basic insights in the intrinsically emitted Ly $\alpha$  properties associated with neutral, collapsing gas clouds. In § 6.2 the dependence of these properties on the other model parameters is studied.

#### 6.1.1. Motivation and Definition of the Four Models.

Our fiducial models have  $M_{\text{tot}} = 5.2 \times 10^{11} M_{\odot}$ ,  $z_{\text{vir}} = 3$  and  $v_{\text{amp}} = v_{\text{circ}} = 180 \text{ km s}^{-1}$ . The choice of these parameters is

based on the redshift 3.0 example presented by Haiman et al. (2000). The four fiducial models differ in the choice of  $\alpha$  and  $j(r)$  and represent the four most extreme cases in the range of physically plausible choices of these parameters. The first two models focus on continuous Ly $\alpha$  emission, which is followed by two models with central Ly $\alpha$  emission.

Models 1. and 2. have  $\alpha = 1$  and  $\alpha = -1/2$ , respectively. Both models have an emissivity profile which is given by equation (11). The total Ly $\alpha$  cooling luminosity is  $\sim 3 \times 10^{42}$  and  $\sim 9 \times 10^{42} \text{ ergs s}^{-1}$  for model 1. and 2., respectively. Converting this to a flux on earth using  $f_{\text{Ly}\alpha} = L_{\text{Ly}\alpha}/(4\pi d_L^2)$ , where  $d_L$  is the luminosity distance to the Ly $\alpha$  source<sup>2</sup>, we get  $f_{\text{Ly}\alpha} = 4.0 \times 10^{-17}$  and  $1.2 \times 10^{-16} \text{ ergs s}^{-1} \text{ cm}^{-2}$ , respectively. These values are very similar to those given in Haiman et al. (2000), who obtained  $f_{\text{Ly}\alpha} = 4.2 \times 10^{-17} \text{ ergs s}^{-1} \text{ cm}^{-2}$ , based on the total available gravitational binding energy and the timescale over which the object is allowed to cool and collapse.

Models 3. and 4. are identical to models 1. and 2., respectively, with  $j(r) \propto \delta(r)$ . The procedure used to generate and subsequently transport individual Ly $\alpha$  photons is described in § 3.1. The edge of the sphere,  $r_{\text{max}}$ , is at the virial radius. We first describe the main results of the calculations below in § 6.1.2, which are explained qualitatively in § 6.1.3.

#### 6.1.2. Main Characteristics of Ly $\alpha$ Emission Emerging from the Four Models

The emerging spectrum (*left panels*) and surface brightness profile (*right panels*) for all four models are shown in Figure 5. The top row corresponds to model 1., as we move down one panel we move up one model number. The lower horizontal axis on the left column denotes the usual frequency variable  $x$ , which is converted to a velocity offset (in the Ly $\alpha$  emitter's rest-frame) from the line center, on the top axis. Note that positive values of  $x$  correspond to higher energies, or bluer photons. This higher energy is translated to a lower redshift, or lower recessional velocity. A positive  $x$  corresponds therefore to a negative velocity offset. The vertical axis on the left side has units which are such that the area under the curves corresponds to  $(2\pi)^{-1}$  (similar as in Fig. 2). The vertical axis on the *right panels*, showing the surface brightness profiles, indicates the physical flux density in units of  $\mu \text{ Jy}$ . The horizontal axis denotes the impact parameter, measured in  $''$ . The units of the surface brightness on the vertical axis are  $\text{ergs s}^{-1} \text{ cm}^{-2} \text{ arcsec}^{-2}$ . The thick dotted horizontal line is the detection limit in the survey done by Matsuda et al. (2004).

First, we focus on the spectra which show that the Ly $\alpha$  radiation escapes the collapsing protogalaxy predominantly blue shifted for all models. The continuous models are redder than the central models, and contain a faint red peak. The location of the maximum of the blue peak in the spectrum of models 1. and 2. is barely affected by the change in  $\alpha$ . The feature in the spectrum that does vary with  $\alpha$  is the blue tail of the blue peak. For  $\alpha = -0.5$  the spectrum contains relatively more photons blueward of the maximum of the blue peak. The spectra of the central models 3. and 4. are strikingly different in two regards: 1) The spectrum as a whole is shifted further to the blue and there is no red peak. 2) The exact location and FWHM of the blue peak are strongly dependent on the value of  $\alpha$ .

<sup>2</sup>Note that this estimate ignores the IGM. The estimate serves mainly as a consistency check with Haiman et al. (2000), who also ignored the IGM. A discussion on how the IGM affects the detectable flux on earth is delayed to § 5.3.

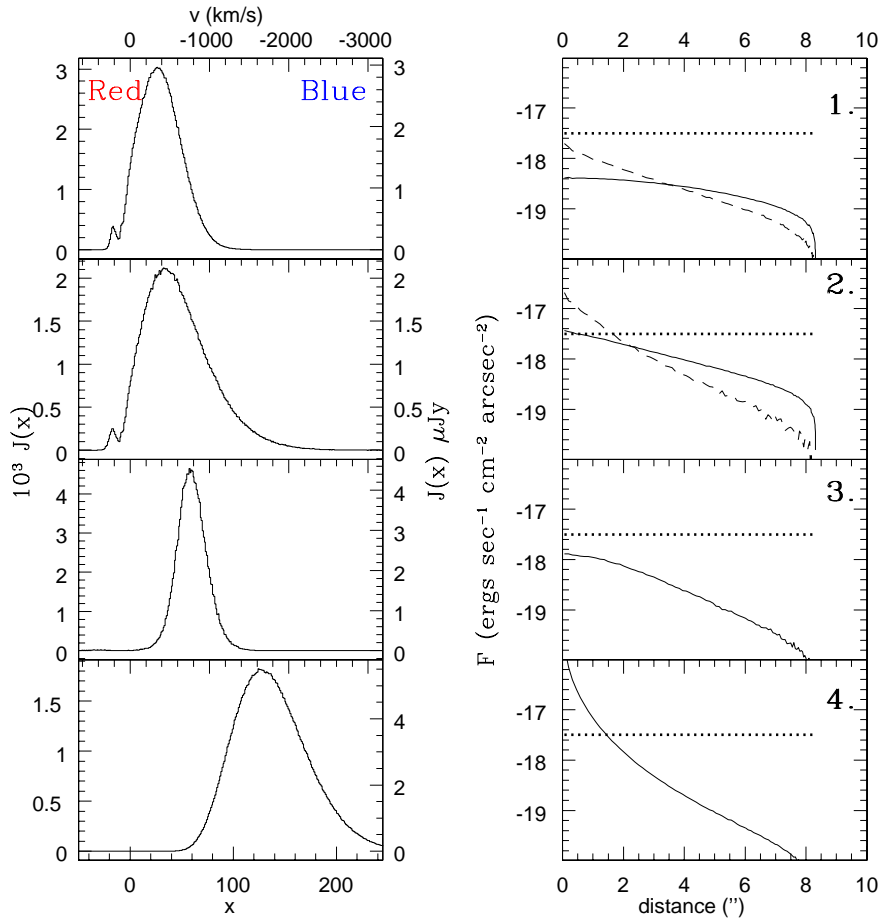


FIG. 5.— Intrinsic properties of the Ly $\alpha$  emission emerging from our four fiducial models (models 1, 2, 3 and 4) of neutral collapsing gas clouds (models 1-4). The *left panels* show spectra in which the bottom x-axis shows the normalized frequency variable  $x$ . The upper x-axis shows what velocity offset this frequency corresponds to. Values of  $x > 0$  correspond to higher frequencies, or lower redshifts, which corresponds to lower recessional velocities. The left y-axis shows the normalized flux, while the right y-axis has the flux density in  $\mu\text{Jy}$ . Processing by the IGM is ignored in the plot. The *right panels* show the surface brightness distribution. The *thick dotted horizontal line* corresponds to the detection limit in a recent survey for Ly $\alpha$  blobs by Matsuda et al. (2004). The model number is shown in the top right corner. The details of each model can be found in Table 1. The *black-dashed line*, in the *upper two panels* in the right column, is the surface brightness profile that would emerge, in the absence of scattering. For the central models, this line corresponds to a  $\delta$ -function at 0", and is therefore not shown.

Second, we focus on the surface brightness distribution. Model 1. has a very flat profile,  $F(\theta) \propto \theta^{-a}$ ,  $a \sim 0.5$ . Model 2. has a steeper profile with  $a \sim 1.0$ . Overplotted as the *dashed line* is the profile that would emerge in the absence of scattering. The purpose of this line is that it illustrates to what extent the surface brightness distribution becomes shallower because of scattering. The profiles for models 3. and 4. are more centrally concentrated ( $a \sim 2$ ), which can be viewed simply as an extension of the trend seen in the profiles of models 1. and 2.: A steeper emissivity profile translates to a steeper surface brightness profile.

### 6.1.3. Physical Interpretation of Main Characteristics

The main goal of the discussion below is to explain the trends described above. The first observation that the Ly $\alpha$  comes out predominantly blueshifted has two reasons: 1) Photons propagating outwards in a collapsing gas cloud experience a net blueshift: According to equation (3),  $\vec{v}_a \cdot \vec{k}_i$  is negative ( $\vec{v}_a$  and  $\vec{k}_i$  are anti-parallel for photons that are propagating outwards), while  $\vec{v}_a \cdot \vec{k}_o$  is 0 on average, which results in  $x_0 > x_i$ . 2) Blueshifted Ly $\alpha$  photons that are propagating outwards appear even bluer (and thus further in the wing) for the infalling gas, which facilitates their escape, while the reverse is true for redshifted pho-

tons. These two effects yield a suppressed red and enhanced blue peak (ZM02). The latter also offers an explanation for the minimum in the spectra of models 1. and 2. around  $x \sim -13$ . When these photons are propagating outwards, they are at resonance in the frame of the infalling gas, which significantly reduces their escape probability. The minimum of the spectrum may therefore be viewed as a measure of the gas' infall velocity (at the outermost gas shells).

All other observations can be explained simultaneously. Decreasing  $\alpha$  increases  $v_{\text{bulk}}(r)$  at small radii, which, according to equation (3) affects the change in frequency  $x$  per scattering. Figure 6 shows the volume averaged scattering redistribution function (§ 2) between  $r = 0.1 - 0.2r_{\text{max}}$  for  $x = 0$ , with  $\alpha = -0.5$  (*red-dotted line*) and 1.0 (*black-solid line*). Clearly, the redistribution functions differ dramatically for  $\alpha = 1.0$  and  $\alpha = -0.5$ . The difference is understood from equation (3), which shows that  $\Delta x \equiv x_i - x_o \sim \vec{v}_a \cdot (\vec{k}_o - \vec{k}_i) / v_{\text{th}}$ . Therefore,  $\Delta x$  lies in the range  $\Delta x \in [-2v_{\text{bulk}}/v_{\text{th}}, 2v_{\text{bulk}}/v_{\text{th}}]$ . For  $r \in [0.1r_{\text{vir}}, 0.2r_{\text{vir}}]$ ,  $v_{\text{bulk}}$  is  $\sim 2v_{\text{amp}}$  and  $\sim 0.15v_{\text{amp}}$  for  $\alpha = -0.5$  and  $\alpha = 1.0$ , respectively. This shows that the range in  $\Delta x$  should be much larger for  $\alpha = -0.5$  which is exactly the message Figure 6 conveys. The photons that escape from the central regions are spread

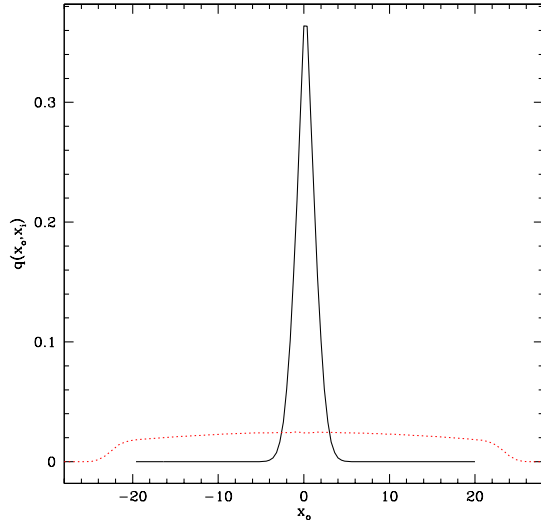


FIG. 6.— The volume averaged redistribution function  $q(x_o, x_i)$  for  $r \in [0.1, 0.2]r_{\text{max}}$  and  $x_i = 0$ . The strongly peaked function is associated with model 1., that has  $\alpha = 1.0$ , while the other is associated with model 2., in which  $\alpha = -0.5$ . The difference is due to the different gas dynamics.

over a much larger range of frequencies  $x$ . This is clearly the mechanism that drives the photons into the blue tail (also into the red tail, but these photons get scattered in the infalling gas).

For the gas distribution used in these models, a large fraction of the total optical depth from the center to the edge of the sphere, comes from the inner regions. In this particular model, half of the contribution to the total column of hydrogen,  $N_{\text{HI}} \sim 3 \times 10^{21} \text{ cm}^{-2}$  comes from  $r \lesssim 0.07r_{\text{vir}}$ . Photons injected in the high density center of the sphere, undergo the majority of resonant scattering events in the high density core. Therefore, all photons in the central models, are subject to the gas kinematics in the center of the sphere, which explains the strong dependence of their emerging spectrum at the surface on  $\alpha$ .

All  $\text{Ly}\alpha$  photons injected in the central regions (in both the continuous and central models), need to work their way out to the edge of the sphere, which causes them to experience a net blueshift. According to equation (3) the amount of blueshift increases with infall velocity and therefore with decreasing  $\alpha$ . In the continuous cooling cases,  $\alpha = -0.5$  boosts the emission from small values of  $r$ . Since these photons are most likely to arrive at the surface with a large blueshift, this explains the enhanced blue tail of the spectrum of model 2., compared to that of model 1. (note that additional support for this will be given in § 6.2.2). It also explains the dependence of the location of the maximum of the blue peak on  $\alpha$  for the central models, since all photons undergo the net blue shift. Additionally, it explains their lack of  $\text{Ly}\alpha$  photons that reach the surface of the sphere with a redshift. The faint red peak in the continuous models is therefore composed mainly of photons that were emitted at large radii and did not undergo a large net blue shift. Therefore, the red peak is not affected by the gas kinematics in the central regions and, consequently, the exact value of  $\alpha$ . The fact that the redistribution function is much broader for  $\alpha = -0.5$  allows photons to be scattered into a wider range of frequencies and also explains the increased FWHM of the blue peak for  $\alpha =$

$-0.5$ .

The enhanced surface brightness in the center suggests that some fraction of the photons can stream freely from the center through the outer gas shells. This fits in well with the scenario sketched above in which the blue tail consists of photons that experience their large blue shift in the central region of the sphere. Their large separation from the line's resonance allows a fraction of the photons in the blue tail to stream freely from the center through the outer shells of the sphere (Note that for  $x = 70$ ,  $\tau_x \sim 1.8 \times 10^{-8}\tau_0$ , whereas the column of hydrogen from edge to center for this model is  $\sim 3 \times 10^{21}$ , which for a static cloud corresponds to  $\tau_0 \sim 1.8 \times 10^8$ ).

The previous discussion can be summarized by stating that the  $\text{Ly}\alpha$  photons emitted in the central regions emerge predominantly blueshifted, often experiencing their last scattering in the center, after which they propagate freely through the outer shells. The photons that emerge with a net redshift are mainly emitted and scattered in the outer regions.

## 6.2. A Closer Look at $\text{Ly}\alpha$ Features in a Suite of Models

The main purpose of this section is to confirm the conclusions and to uncover potential correlations that were not noticed in the discussion of the four models above.

### 6.2.1. Spectral Shape: Peak Morphology

#### The Red Peak.

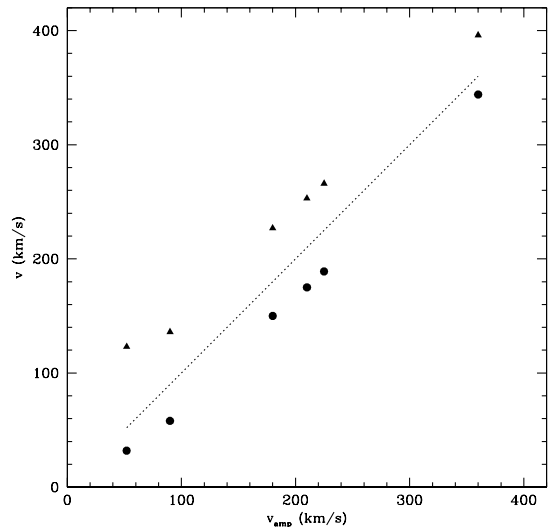


FIG. 7.— The location of the maximum of the red peak (filled-circles) and the minimum in the spectrum (filled-triangles) as a function of  $v_{\text{amp}}$ . The dotted line corresponds to the curve  $v = v_{\text{amp}}$ . Despite the fact that the included models (models 1, 13, 14, 22, 43 and 91) vary in mass, redshift and  $\alpha$ , the correlation is obvious, which suggests it is a generic property of the continuous models.

We found in §6.1.2 that the location of the maximum of the red peak and especially the minimum in the spectrum, also referred to as the ‘dip’, are a measure of the infall velocity of the gas. To verify this, we plot the location of the dip and the peak as a function of the amplitude of the velocity field for various models in Figure 7 as triangles and filled circles respectively. Shown dotted is the line  $v = v_{\text{amp}}$ . Models 91., 13. and 14. only

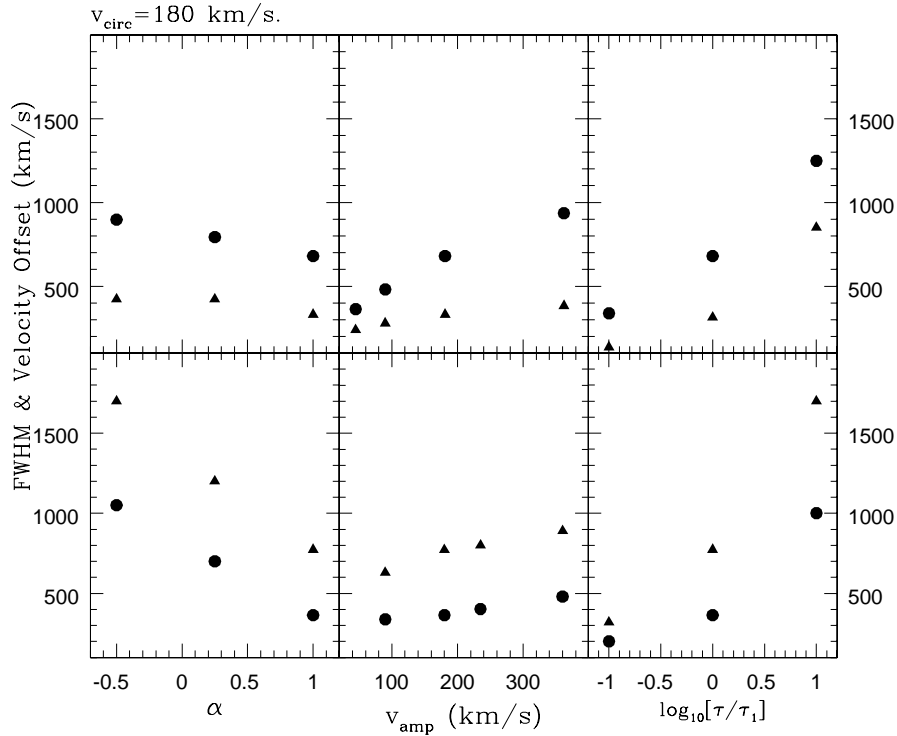


FIG. 8.— This figure shows the morphology of the blue peak as a function of various model parameters. The location of the maximum of the blue peak *filled-triangles* and its FWHM (*filled circles*) as a function of 3 parameters for the continuous (*upper panel*) and central (*lower panels*) models. The *left panel*, *middle panel* and *right panel* shows the dependence on  $\alpha$ ,  $v_{\text{amp}}$  and the optical depth  $\tau$ . The optical depth  $\tau$  is normalized to  $\tau_1$ , which is the optical depth from center to edge of model *I*. (see text). Both the location of the maximum and the FWHM of the blue peak are determined by a combination of the velocity of the infalling gas and the total column of hydrogen from the center to the edge of the object.

differ from model *I*. in their values of  $(v_{\text{amp}}, \alpha)$ , whereas models 22. and 43. have a different redshift and  $M_{\text{tot}}$ , respectively. The exact parameters used for these models used in the plot can be read off from Table 1.

The relation between  $v_{\text{amp}}$  and the location of the peak and dip is evident, although we caution that beyond  $v_{\text{amp}} \sim 360 \text{ km s}^{-1}$  the correlation breaks down. The reason is that the red and the blue peak start to overlap. As will be shown below, the FWHM of the blue peak increases with  $v_{\text{amp}}$ , and for sufficiently large values of  $v_{\text{amp}}$ , the blue and red peaks merge. The correlation holds for a wide range of models, which we take as evidence for it being a generic property of the continuous models.

### The Blue Peak

The morphology of the blue peak such as the location of its maximum in frequency (*as filled triangles*) and its FWHM (*as filled circles*) are shown in Figure 8 as a function of three parameters:  $\alpha$ ,  $v_{\text{amp}}$  and the optical depth  $\tau$  from the center to the edge of the object. The top row of panels represents continuous cooling models, while the bottom row represents the same models, with  $j(r)$  changed to central.

First we focus on the two *left panels* in Figure 8. The *upper left panel* shows the location of the maximum of the blue peak and its FWHM, for the continuous models *I*., 2. and 57. that have  $\alpha = -0.5, 0.25$  and 1.0, respectively. The dependence of the location of the maximum on  $\alpha$  is weak, while its FWHM is slightly more dependent on  $\alpha$  (which is not surprising, as

we noticed that the blue tail was more pronounced in model 2. than in model *I*.). On the other hand, the *lower left panel* shows that for the central cases, the dependence on  $\alpha$  is very strong. This is the first big difference with the continuous models. The second is that the FWHM is less than the velocity offset of the maximum of the blue peak. Note that this is also evident from the lower two rows in Figure 5. An explanation of these features is given following the description of the *central panels*, which show the location of the maximum and FWHM of the blue peak a function of  $v_{\text{amp}}$  for the continuous (*upper panel*) and central models (*lower panel*). For the continuous models the FWHM depends more strongly on  $v_{\text{amp}}$  than on the peak's location. For the central models the dependence of both quantities on  $v_{\text{amp}}$  is weak. Also, the dependence of the FWHM on  $v_{\text{amp}}$  for these models is slightly weaker relative to that of their continuous counterparts.

The trends mentioned above, can be understood from the impact of  $v_{\text{bulk}}$  on the redistribution function. As we showed in § 6.1.2 and Figure 6, the change in the Ly $\alpha$  photon's frequency per scattering, lies in the range  $\Delta x \in [-2v_{\text{bulk}}/v_{\text{th}}, 2v_{\text{bulk}}/v_{\text{th}}]$ . Changing  $\alpha$  from 1.0 to  $-0.5$ , causes  $v_{\text{bulk}}$  to be enhanced by a factor of  $(r_{\text{vir}}/r)^{1.5}$ , which can become very large at small radii. Note that for  $\alpha = -0.5$ , the maximum infall velocity is limited to  $2v_{\text{circ}}$ , see § 5.2. Since *all* photons in the central models are subject to the gas kinematics in the central regions, the strong dependence of the morphology of the blue peak on  $\alpha$  for the central cases can be understood. The weaker dependence on  $v_{\text{amp}}$ , for the central models, is because  $v_{\text{amp}}$  is varied by a factor of at most 4, which boosts the bulk velocity of the gas at

small  $r$  less than is accomplished by lowering  $\alpha$ . Similarly, a large fraction of the photons emitted in the continuous models are not subject to the changed dynamics in the center at all, which explains the weak dependence on  $\alpha$ .

For the models considered here, which have  $\alpha = 1.0$ , changing  $v_{\text{amp}}$  affects the redistribution function strongest at large radii. Because scattering in the outer shells is relatively more important for the continuous models, the FWHM of their emerging blue peak is more strongly affected by  $v_{\text{amp}}$ . The location of the maximum of the blue peak appears to vary less with  $v_{\text{amp}}$  than for the central cases. This is most likely due to the overall increased blue shift of the blue peak in the central models: the relative increase for both set of models, from 90–360 km s<sup>-1</sup> is comparable.

The maximum of the blue peak is affected by a third parameter. As discussed in § 2, in a static sphere, the location of the maximum of both peaks is set by the total optical depth from the center to the edge of the sphere. The effect of bulk motions was mainly to suppress one and enhance the other of the two peaks. The total optical depth from the center to the edge of the sphere should therefore affect the location of the maximum of the blue peak. The *right panels* of Figure 8 shows the location of the maximum of the blue peak and its FWHM for three different optical depths,  $\tau$ . The optical depth is normalized to that of model 1., denoted by  $\tau_1$ . All models are identical in their dark matter and gas properties, but the Ly $\alpha$  absorption cross section is decreased and increased by a factor of 10 for the point with  $\tau/\tau_1 = 0.1$  and 10.0, respectively. The figure demonstrates clearly that the blue peak’s morphology is strongly affected by the value of  $\tau$ .

Unlike the case for the red peak, the morphology of the blue peak is not uniquely determined by the infall velocity of the gas. We found it to be determined by a combination of the kinematics of the infalling gas and the total optical depth from the edge to the center of the sphere. This suggests that accurately measuring both the FWHM and the location in frequency of the blue peak might put constraints on both the gas kinematics and the total column of hydrogen gas. Given the simplified nature of our models, however, it is not possible to quantify this in detail.

### The Blue to Red Ratio

Some emphasis has been put on the presence of a tiny red peak in the spectra of models that undergo continuous Ly $\alpha$  cooling. This red peak, if detectable, would contain robust information on the infall velocity of the cooling gas. In this paragraph a more systematic study is performed on the presence and prominence of the red peak in models with different masses, velocity fields, redshifts and emissivity profiles. The prominence of the red peak is quantified through the blue to red ratio,  $[B]/[R]$ , which is defined as the ratio of the number of photons in the blue and red peak. The transition between the two is at the minimum in the spectrum.

First we demonstrate how the transition occurs from a double peaked symmetric spectrum, known from the static cases, to the asymmetric spectra, that are associated with bulk motions. The *left and right panel* of Figure 9 contains the (normalized) spectrum of models 1. and 3., respectively, as the *black–solid lines*. The *red–dotted lines* correspond to the same models, in which the amplitude of the infall velocity has been reduced to  $0.25v_{\text{circ}}$ . The *blue dashed lines* correspond to  $v_{\text{amp}} = 0$  (actually,  $v_{\text{amp}} = 10^{-6}v_{\text{circ}}$ , because for  $v_{\text{amp}} = 0$  there is no emission

for the continuous cases according to eq. 11).

The slight asymmetry that is present in both static cases, is intriguingly enough, due to deuterium. Deuterium also leaves a sharp feature at  $x = x_D$  in the static, continuous, case. The effect of deuterium on the other spectra was found to be negligible. Figure 9 shows that  $[B]/[R]$  increases strongly with  $v_{\text{amp}}$  for both the central and continuous models. In the central cases, the blue and red peak remain well defined and separated as the amplitude of the infall velocity is turned on, until ultimately the amplitude of the red peak is zero. For the continuous cases, the FWHM of the blue peak increases, and that of the red peak decreases, until the peaks merge. Additionally, the minimum in the spectrum that separates the blue and the red peak moves to the left (and is a direct measure of the gas’ infall velocity, as shown in Fig. 7).

Figure 10 shows the exact value of  $[B]/[R]$  as a function of  $z_{\text{vir}}$ ,  $v_{\text{amp}}$ ,  $\alpha$  and  $M_{\text{tot}}$ . The *filled circles* refer to the continuous models, whereas the *open stars* refer to the central models. The *bottom-left panel* shows  $[B]/[R]$  as a function of  $\alpha$ . For the continuous models  $[B]/[R]$  is relatively insensitive to the value of  $\alpha$ . The main effect of varying  $\alpha$  was to enhance the blue tail of the blue peak in the continuous models (§ 6.1.2). The top left two plots in Figure 5 show that the enhancement of the blue tail is at the expense of photons in the other part of the blue peak: The normalized spectrum for  $\alpha = -0.5$  has a lower maximum flux density. Therefore, varying  $\alpha$  mainly redistributes photons in the blue peak, which leaves  $[B]/[R]$  roughly constant. For the central models, the only finite value of  $[B]/[R]$  was measured for  $\alpha = 1.0$ . As shown in the bottom two panels of Figure 5, decreasing  $\alpha$  pushes the blue peak further into the blue, reducing the probability that a red photon can escape.

The *bottom-right panel* shows the value of  $[B]/[R]$  as a function of the amplitude of the velocity field  $v_{\text{amp}}$ . As mentioned above (and in § 6.1.2), increasing  $v_{\text{amp}}$  increases  $[B]/[R]$ . Note that for sufficiently large  $v_{\text{amp}}$ , the FWHM of the blue peak for the continuous models can be such that the red peak is absorbed in the blue peak, in which case  $[B]/[R] \rightarrow \infty$ . The *top-left panel* shows  $[B]/[R]$  as a function of mass. The effect of varying mass is twofold: 1) The circular velocity, and therefore the infall velocity of the gas, increases with mass. 2) The total column of

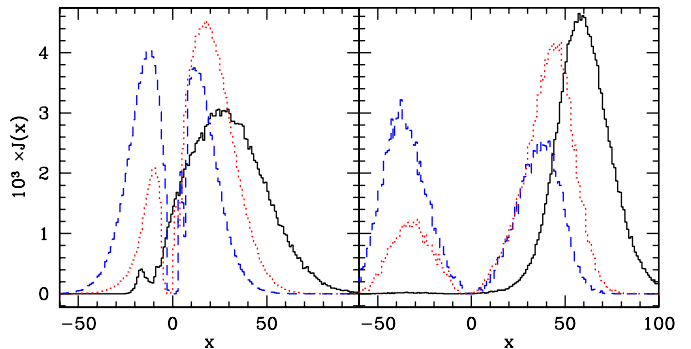


FIG. 9.— The effect of bulk motions in the gas on the emerging Ly $\alpha$  spectrum is shown for the continuous (*left panel*) and central (*right panel*) cases. The panels contain normalized spectra for three models that only differ in the amplitude of the velocity field. The *black–solid lines* in the left/right panel corresponds to model 1./3., respectively. The *red dotted lines* correspond to the same models with  $v_{\text{amp}}$  reduced to  $0.25v_{\text{circ}}$  (models 14 and 59). The *blue dashed line* corresponds to static models,  $v_{\text{amp}} = 0$  (models 99 and 58).

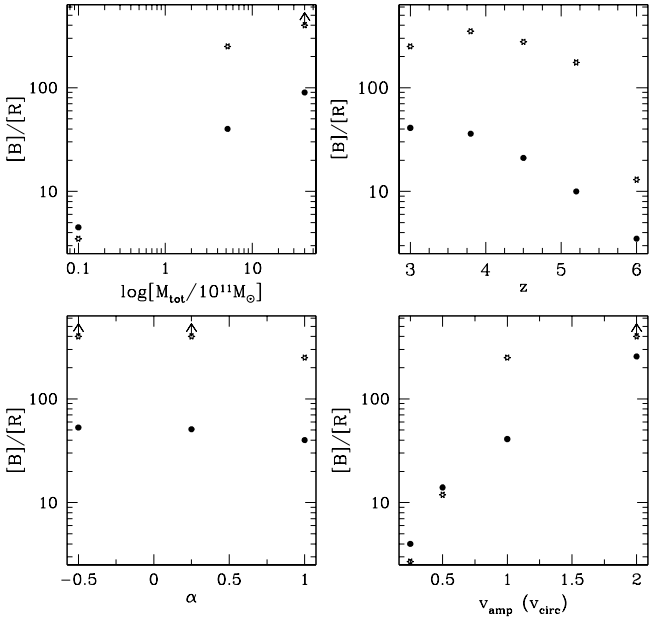


FIG. 10.— The ratio of the number of photons *intrinsically emitted* in the blue and red peak,  $[B]/[R]$ , as a function of various parameters. The fiducial model is model 1. (see Table 1). Variation with: *Upper left panel*: Mass, *Lower left panel*:  $\alpha$ , *lower right panel*:  $v_{\text{amp}}$ . The redshift dependence in the *Upper right panel* is the *observed* value of  $[B]/[R]$  to emphasize the impact of the IGM.

hydrogen from center to edge of the sphere increases with mass, which affects the FWHM and location of the blue peak (Fig. 8). Both effects result in the increase of  $[B]/[R]$  with mass. The ratio  $[B]/[R]$  for the central models (indicated by the *open stars*) becomes comparable to (and sometimes even lower than) that for the continuous cases for low masses ( $M = 10^{10} M_{\odot}$ ) and low  $v_{\text{amp}}$  ( $v_{\text{amp}} \leq 0.5 v_{\text{circ}}$ ).

The *top-right panel* shows the dependence of  $[B]/[R]$  on  $z_{\text{vir}}$ . The intrinsically emitted spectrum is not varying strongly with  $z_{\text{vir}}$ , since  $z_{\text{vir}}$  only affects the virial radius and circular velocity of model 1.. For the models considered, the amount by which  $v_{\text{circ}}$  varies between  $z = 3$  and  $z = 6$ , is only a factor of 1.3, which is much less than the variation studied in the bottom right panel. The main reason why redshift leaves a strong imprint on  $[B]/[R]$  is the IGM. For this reason, the *observable* value of  $[B]/[R]$  is plotted (including the factor  $\langle e^{-\tau} \rangle$ ), instead of its intrinsically emitted value, as in the other three panels. A discussion of how the IGM was incorporated is delayed to Paper II. Putting aside the details of this modelling, the trend displayed in the plot is easily understood: stronger IGM absorption towards higher redshift decreases the relative number of photons in the blue peak which reduces  $[B]/[R]$ .

### 6.2.2. The Surface Brightness Profile

Here, we focus on the impact of varying the input parameters on the emerging surface brightness profile. We found that the slope of the surface brightness profile was correlated with  $j(r)$  and the value of  $\alpha$  in §6.1.2. Figure 11 shows the surface brightness distribution as a function of  $M_{\text{tot}}$ ,  $\alpha$  and  $j(r)$ . The *top and bottom panels* are associated with continuous and central models, respectively. Each panel contains three models for one particular mass,  $M_{11}$ , which is given in the top right corner in units

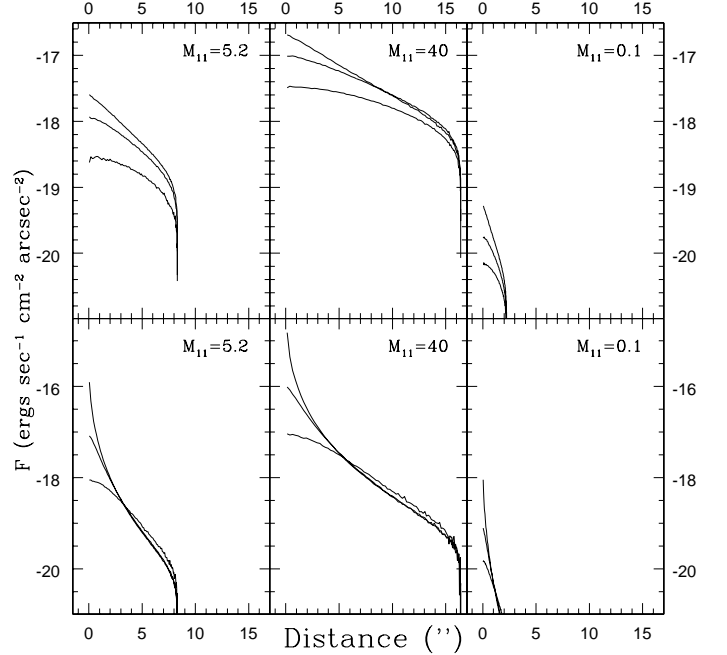


FIG. 11.— The surface brightness as a function of angular distance in '' from the center of the Ly $\alpha$  image. The *top and bottom panels* represent continuous and central models, respectively. Each panel corresponds to a different mass, which is given in units of  $10^{11} M_{\odot}$  in the upper right corner of each panel. The three curves represent models with  $\alpha = -0.5, 0.25$  and  $1.0$ . The steepest and shallowest curves have  $\alpha = -0.5$  and  $\alpha = 1.0$ , respectively.

of  $10^{11} M_{\odot}$ . In all panels, the lowermost and uppermost curve corresponds to  $\alpha = 1.0$  and  $-0.5$ , respectively (also see Fig. 5), the middle curve has  $\alpha = 0.25$ . Figure 11 shows that the surface brightness profile steepens with decreasing mass. The curves in the *middle* ( $M = 4 \times 10^{12} M_{\odot}$ ) and *right panel* ( $M = 10^{10} M_{\odot}$ ) are the flattest and steepest, respectively. There are two reasons for this: 1) The projected emissivity on the sky becomes increasingly shallow with mass, which is due to the mass dependence of the virial radius<sup>3</sup>. 2) The Ly $\alpha$  optical depth increases with mass. This can be seen from the *lower panels* with the central models. Here, the steepness of the profile is regulated solely by the optical depth.

As we also found in §6.1.2 the surface brightness profile steepens with decreasing  $\alpha$  and is steeper for the central models. The main reason for both these points is that photons emitted in the central regions, are more likely to emerge with a net blue shift, often passing through the outer gas shells in a single flight (see § 6.1.2, § 6.2, for more details).

Here, we provide additional support for this claim in Figure 12. This figure shows two surface brightness profile associated with model 1. in the *left panel* and model 2. in the *right panel*. The two profiles are constructed from the reddest 15% (*red solid line*) and the bluest 15% (*blue dotted line*) of all Ly $\alpha$  photons. The bluest 15% is more concentrated, especially for model 2., which has  $\alpha = -0.5$ . This demonstrates that the bluest photons emerge predominantly from the central regions, while the reddest photons come mainly from the outer parts. Seeing this in the data would be a good indicator of the presence

<sup>3</sup>If the surface brightness profiles were plotted as a function of  $\theta/\theta_{\text{vir}}$ , in which  $\theta_{\text{vir}}$  is the angle the virial radius subtends on the sky, they would be self-similar.

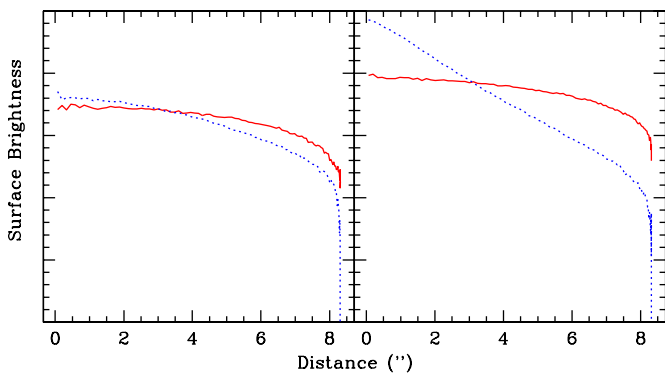


FIG. 12.— This figure shows the frequency dependence of the surface brightness profile for the continuous models. The surface brightness profile for the bluest (dotted blue line) and reddest (red solid line) 15% of the photons are shown. The left and right panel corresponds to models 1. and 2., respectively. The bluest photons emerge more centrally concentrated.

of neutral hydrogen gas that is collapsing while continuously emitting Ly $\alpha$  cooling radiation.

## 7. FLUORESCENT LY $\alpha$ EMISSION FROM SELF-IONIZED PROTOGALAXIES

As mentioned in § 1, the total Ly $\alpha$  emissivity can be greatly boosted by embedded ionizing sources. A requirement for this boost, however, is that the gas is clumpy, which increases the recombination rate and allows a larger fraction of the ionizing radiation to be reprocessed into Ly $\alpha$  photons, rather than escaping, e.g. (Partridge & Peebles 1967; Haiman & Rees 2001; Alam & Miralda-Escudé 2002). Because clumpiness is not included in our model, this boost in the Ly $\alpha$  luminosity is not achieved. In this section, we focus on the other observable properties of fluorescent Ly $\alpha$ , such as its surface brightness distribution and its spectrum. For this purpose, an ionizing point source was inserted at the center of our sphere. Its total flux in ionizing photons is  $L_{\text{ion}}$  (in ergs s $^{-1}$ ) and its spectrum is a power law of the form  $J(\nu, r) = J_0(r)(\nu/\nu_L)^\beta$  in ergs s $^{-1}$  cm $^{-2}$  sr $^{-1}$ . The slope  $\beta$  depends on the nature of the ionizing sources. We choose  $\beta = 1.7$ , for the point source to represent a quasar. The value of  $J_0(r)$  is obtained by  $J_0(r) = (\beta - 1)L_{\text{ion}}/[16\nu_L\pi^2r^2]$ . The standard equations of photoionization equilibrium were solved numerically with the code. The optical depth to the first shell was assumed to be 0. This was used to calculate its neutral fraction of hydrogen. This allows the optical depth to the next shell to be computed, which also determines its neutral fraction. This procedure is repeated until the outer shell is reached. The resulting changes in the intrinsically emitted Ly $\alpha$  spectrum are presented below.

### 7.1. Impact of a Central Ionizing Source on the Properties of the Emerging Ly $\alpha$ Emission

We insert an ionizing source in the center of model 1. (see Table 1). The Ly $\alpha$  photons that are created in response to the photo-ionizing flux from the central quasar, are added to those produced by cooling radiation:

$$j(r) = \mathcal{F}_\alpha \alpha_B [1 - x_H(r)]^2 n_H^2(r) h\nu_0 + f_\alpha \frac{G M_{\text{tot}}(< r) \rho_b}{r^2} \frac{dr}{dt} \quad (15)$$

where  $\mathcal{F}_\alpha$  is the average number of Ly $\alpha$  photons produced per recombination, which is  $\sim 68\%$  in the regime which is optically thick to UV photons, and  $\sim 42\%$  in the optically thin regime. The second term is the same as used for the continuous cooling models (eq. 11). The main reason for keeping this term is to make the transition from the previous continuous models to the current models smoother.

The gas in model 1. becomes fully ionized at  $L_{\text{ion}} = 10^{43}$  ergs s $^{-1}$ . We caution again that this estimate ignores small-scale gas clumping. If we denote the clumping factor by  $C \equiv \langle \rho^2 \rangle / \langle \rho \rangle^2$ , then this transition to full ionization occurs at  $\sim C$  times higher ionizing luminosity (which would allow for  $\sim C$  times higher Ly $\alpha$  luminosity). Increasing  $L_{\text{ion}}$  beyond this value, merely reduces the residual neutral fraction, and consequently,  $N_{\text{HI}}$ .

The ‘phase transition’ from neutral to fully ionized dramatically affects the emerging Ly $\alpha$  spectrum. In Figure 13 we show the Ly $\alpha$  spectrum and surface brightness distribution for three values of  $L_{\text{ion}}$ :  $L_{\text{ion}} = 0$  (black–solid line),  $L_{\text{ion}} = 5 \times 10^{42}$  ergs s $^{-1}$  (red–dotted line),  $L_{\text{ion}} = 10^{43}$  ergs s $^{-1}$  (blue–dashed line) and  $L_{\text{ion}} = 10^{46}$  ergs s $^{-1}$  (green–long–dashed line). The results are presented differently than above: The left panel shows the surface brightness distribution rotated by 90°. The right panels show spectra of these models at four different impact parameters,  $\theta$ , indicated by the horizontal dotted lines. For example, the lowest panel shows the spectrum emerging from  $\theta \sim 0-2''$ , the second lowest panel shows the spectrum emerging from  $\theta \sim 2-4''$ , etc. The main reason for presenting the data in this fashion is to study the variations in the spectra across the object. Note that the spectra are arbitrarily normalized for visualization purposes.

We note that in the absence of an ionizing source, the spectrum (black–solid line) is fairly constant across the object, the central region being slightly bluer. For low ionizing luminosities,  $L_{\text{ion}} = 5 \times 10^{42}$  ergs s $^{-1}$ , photo-ionization enhances the Ly $\alpha$  emission from the central regions. As we learned in § 6.1.2, enhanced emission in the center enhances the number of photons in the bluest parts of the spectrum, and steepens the surface brightness profile. These are indeed the changes that can be seen in Figure 13. The FWHM of the blue peak of the spectra emerging from the two central regions is smaller for the model with the ionizing source (red–dotted line). This resembles the difference in FWHM observed between models 1. and 3. (see Figs. 5 and 8). When  $L_{\text{ion}}$  is increased by a factor of two, the gas sphere as a whole is fully ionized, which has several effects. The spectrum becomes much narrower (blue–dashed line), and centered on a frequency slightly blueward of the line center ( $x \sim 3$ ). The main reason is the reduced column of neutral hydrogen, which reduces the importance of broadening of the Ly $\alpha$  line by resonant scattering. Instead, the broadening is determined by the bulk velocity of the gas, despite the fact that each Ly $\alpha$  photon scatters  $\sim 10^4$  times before it escapes. The main reason that the Ly $\alpha$  spectrum is barely affected by scattering, is that each Ly $\alpha$  photon mainly gets scattered near the site of its creation, where the photon is at resonance. A chance encounter with a rapidly moving atom can put the photon in the wing of the line, which allows it to escape in a single flight from the local resonant region (in which the optical depth is  $\tau_0 \sim 10^3$ ). These photons escape this region in a typical double peaked profile around the local line center. Velocity gradients in the gas facilitate the photon’s escape from the rest of the object. The frequency with which the photon finally emerges at the virial radius therefore does contain information on the bulk

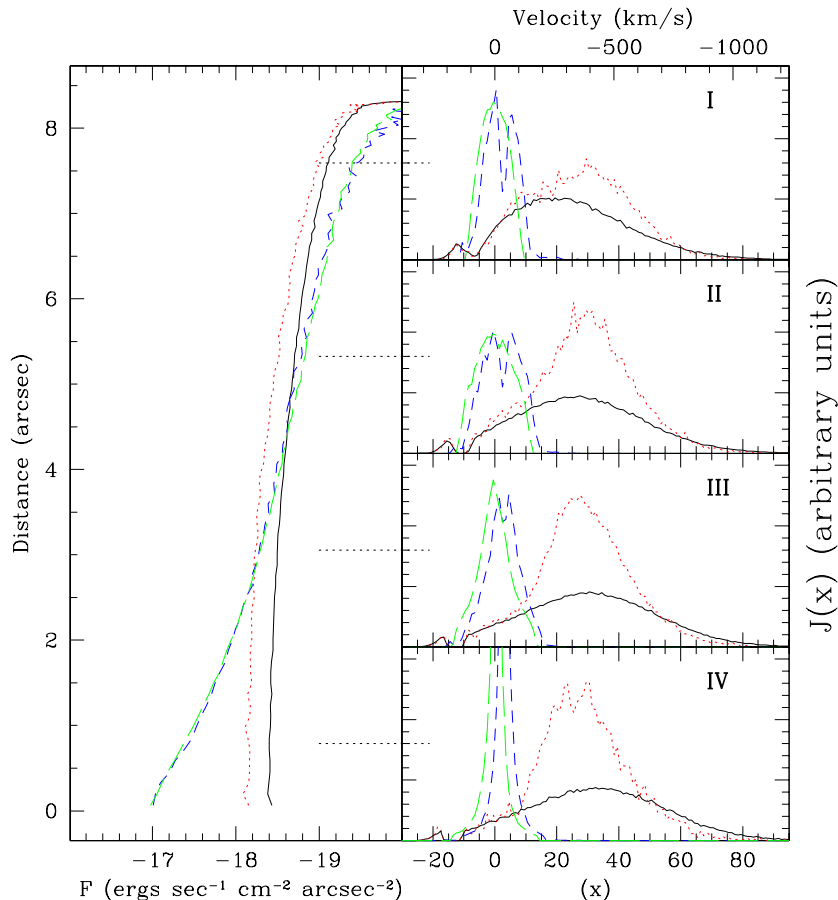


FIG. 13.— This figure displays the effect of a central quasar on the  $\text{Ly}\alpha$  surface brightness distribution and spectra emerging from a collapsing gas cloud for four models. The quasar’s ionizing luminosity is different for each model. The *left panel* shows the surface brightness distribution as a function of impact parameter, measured in  $''$  from the center (Note that the figure is rotated relative to Fig. 5: the angular distance is on the vertical axis). The four panels on the right contain the spectra of the regions of the image, centered on the impact parameter indicated by the *black-dotted lines*. Each panel contains curves that represent four models: Our fiducial model *I*, is represented by the *black-solid line*. The *red-dotted line*, *blue-dashed line* and *green-long-dashed line* corresponds to model *I*, plus an additional central ionizing source with  $L_{\text{ion}} = 5 \times 10^{42}$  ergs  $\text{s}^{-1}$ ,  $L_{\text{ion}} = 10^{43}$  and  $10^{46}$  ergs  $\text{s}^{-1}$ , respectively.

velocity of the site where the photon was generated. The double peak in the emission line is a consequence of this local resonant scattering. The main reason for the enhanced prominence of the dip at large impact parameters is that the velocity gradient projected along the line of sight is smaller there, which increases the total column of hydrogen a  $\text{Ly}\alpha$  photon effectively sees.

The reason that the spectrum from region IV is narrower is that it mainly contains photons that emerge from the central regions, in which the bulk infall velocity is low ( $\alpha = 1.0$ ). The effect of the velocity field and  $L_{\text{ion}}$  on the emerging spectrum is investigated in more detail in § 7.2.

### 7.2. Constraints from $\text{Ly}\alpha$ Emission on Gas Kinematics in the Presence of a QSO

In the previous section § 7.1 we argued that the gas kinematics can be constrained by the  $\text{Ly}\alpha$  emission despite the possibility that the  $\text{Ly}\alpha$  photon scatters up to  $10^4$  times. In this section we show that, although the amplitude of the bulk motions in the gas can be constrained well by the gas, the sign is much harder to determine, since the emerging spectra for infall and outflow are almost identical for fully ionized gas. In this section, there is no contribution from cooling to the emissivity; the second term on the RHS in equation (15) is set to 0. The reason is that

we want the emissivity profiles to be the same for the infall and outflow models (in the outflow model, there is no cooling term).

In Figure 14 we show spectra at four different impact parameters for three different models. The *blue-dashed lines* represent model *I*, containing a central ionizing source with  $L_{\text{ion}} = 10^{43}$  ergs  $\text{s}^{-1}$  (as in Fig. 13). These spectra are compared to the no-scattering profiles, which refer to the profiles that would be observed if the gas were transparent to  $\text{Ly}\alpha$  (shown as *black-solid lines*). The *red-dotted lines* represent a model in which the sign of  $v_{\text{amp}}$  is reversed. Each panel contains the spectra at the impact parameter indicated by the roman numerals in the top-right corner (as in Fig. 13). The only prominent difference between all spectra, is that the models in which scattering occurs are shifted by several Doppler widths relative to the no-scattering spectrum. Infall and outflow models are slightly blue and redshifted shifted, respectively. The reasons for this have been discussed in § 6.1.2.

Although not shown in this paper, we found the surface brightness distributions for the infall and outflow models to be the same (also see ZM02, who found the same). This leads to the conclusion that, for fully photo-ionized gas, the  $\text{Ly}\alpha$  spectrum can be used to determine the velocity dispersion of the gas, despite the presence of residual neutral hydrogen that may scatter each  $\text{Ly}\alpha$  photon up to  $10^3 - 10^4$  times. However, the *sign* of

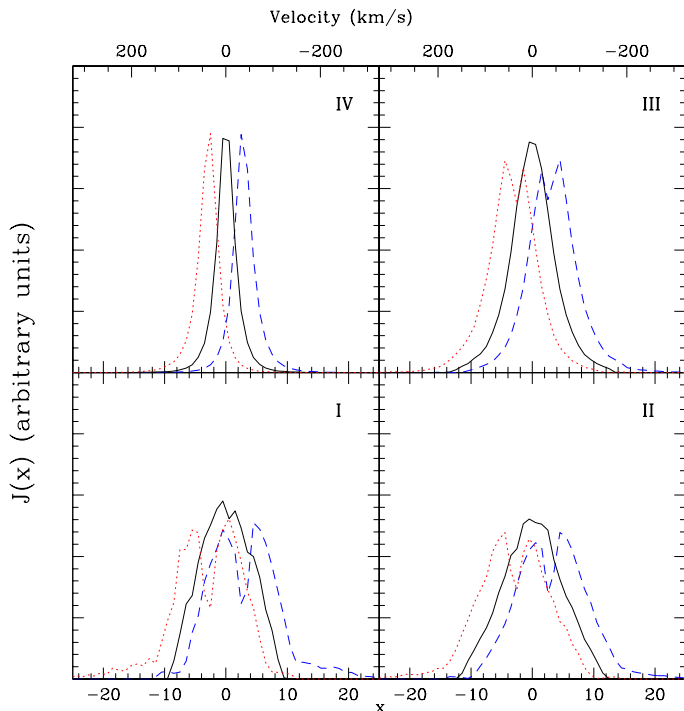


FIG. 14.— The figure illustrates the difference between the intrinsically emitted spectra for outflow and inflow models. Each panel corresponds to the impact parameter indicated by the roman letter (as in Fig. 13). The spectra shown by the *blue-dashed lines* represent a photo-ionized inflow model, while *red-dotted lines* represent the outflow models in which the sign of  $v_{\text{amp}}$  is reversed. The *black-solid lines* represent both inflow and outflow models in the absence of scattering. The figure shows that all spectra are identical except for the small off set in frequency.

the velocity field can only be determined when the exact Ly $\alpha$  line center is known, to an accuracy of  $\sim 10 \text{ km s}^{-1}$  (which is not possible in practice). This may introduce an uncertainty to the recent interpretation by Weidinger et al. (2004, 2005) that their observed Ly $\alpha$  spectrum and surface brightness profile were showing the gas was falling inwards. Our results suggest that the Ly $\alpha$  data is also consistent with an outflow. Weidinger et al. (2004, 2005) argue that the observed lack of metals favor inflow, since outflowing winds would typically be metal enriched.

## 8. DISCUSSION

The gas temperature in this paper was assumed to be  $10^4 \text{ K}$ . The gas temperature affects the r.m.s frequency change per scatter, and therefore affects the results in which the broadening and blueshift of the Ly $\alpha$  emission line are dominated by resonant scattering. However, the temperature dependence of our results is weak. This is best illustrated with an example in which the emergent spectrum is entirely determined by resonant scattering: for a static, uniform sphere, in which Ly $\alpha$  is injected in the center at  $x = 0$ , the emergent spectrum peaks at  $x_p = \pm 0.92(a\tau_0)^{1/3}$  (§ 2). For a fixed total column of hydrogen from the center to the edge of the sphere, we can write the velocity offset from the line center of the two peaks as:  $v_{\text{shift}} \propto T^{1/6}$ . Turbulent motions in the gas may raise the effective temperature of the gas. ZM02 therefore used  $T \sim 10^5 \text{ K}$ . Raising  $T$  to  $10^5 \text{ K}$ , only slightly affects our results quantitatively.

The simplified nature of our models clearly introduces un-

certainties to the results presented in this paper. Nevertheless, several results obtained in this paper should be robust. The conclusion that Ly $\alpha$  emerges blue-shifted from a collapsing cloud will not change for different gas distributions, since it simply relies on Ly $\alpha$  photons encountering gas with a bulk velocity that opposes their propagation direction. The only requirement is that the Ly $\alpha$  photons do meet gas on their way out. If the gas is very clumpy, and only covers part of the sky from the site where the Ly $\alpha$  is generated, then it could escape without a net blue shift. For the massive protogalactic halos considered in this paper the covering factor is expected to be well above one, and we do not expect Ly $\alpha$  to escape without encountering any gas. As argued by Birnboim & Dekel (2003), virial shocks may be absent in halos with  $M_{\text{crit}} \lesssim 2 \times 10^{11} M_{\odot}$ , which suggests that even if the gas is clumpy, in the protogalactic phase, the clumps are not embedded in a hot tenuous medium for masses below  $M_{\text{crit}}$ . Although the mass of our fiducial model lies slightly above this quoted critical mass, its exact value depends on redshift, metallicity of the gas, etc. In this case the gas is also optically thick to Ly $\alpha$  photons between the denser clumps, making our calculations more appropriate.

Similarly, that the bluest photons can freely stream outwards through a column of collapsing gas, while the reddest photons get scattered in the outermost regions, should be valid regardless of the exact gas distribution. It is not clear however, what fraction of centrally produced Ly $\alpha$  escapes. The presence of even a small amount of dust is sufficient to absorb Ly $\alpha$  photons (Neufeld 1990, Charlot & Fall 1991). If the medium is clumpy, then Ly $\alpha$  photons may still escape by scattering of (dusty) cold clouds embedded in a tenuous medium (Neufeld 1991; Haimes & Spaans 1999; Hansen & Oh 2005). The red peak, which is produced further out, suffers less from dust absorption. The net effect of destroying preferentially the bluer photons would weaken the spectral dependence of the surface brightness distribution for the continuous models.

The more detailed results, such as the peak morphology, are very likely to change for realistic gas configurations. For reliable detailed predictions, we should apply the code to the output of cosmological simulations which can provide the Ly $\alpha$  code with realistic density, velocity and temperature fields. The results presented in this paper provide a good sanity check for future results that will be obtained from more complex calculations.

## 9. SUMMARY AND CONCLUSIONS

We presented Ly $\alpha$  Monte Carlo radiative transfer calculations through neutral (§ 5), and self-ionized (§ 7), collapsing, spherically symmetric gas clouds. To provide a test case for our code that is tailored to spherical symmetry, we derived a new analytic solution for the Ly $\alpha$  spectrum emerging from a uniform, static sphere (§ 3.2, Appendix B). We found that a cosmological abundance of deuterium regulates the transfer of Ly $\alpha$  photons over a narrow frequency range (corresponding to  $40\text{--}50 \text{ km s}^{-1}$  at  $T = 10^4 \text{ K}$ , § 4). Although the results in the present paper are not affected by the presence of deuterium, we point out it may affect the analysis for systems with hydrogen column densities in the range  $10^{18}\text{--}10^{20} \text{ cm}^{-2}$ , for  $T = 10^4 \text{ K}$ .

We studied the effects of gas kinematics on the Ly $\alpha$  emissivity as a function of radius as well as various features in the intrinsically emitted spectrum and surface brightness distribution, for a range of models with different masses and redshifts (§ 6.2), which are summarized in Table 1. The ‘continuous

models' are inspired by cooling flow models in which Ly $\alpha$  photons are generated at all radii, with the rate proportional to rate at which the gravitational binding energy changes (but could represent other scenarios in which the Ly $\alpha$  emissivity is spatially extended). The 'central models', although initially motivated by an alternative scenario for cooling radiation, can represent any model in which a strong Ly $\alpha$  emitter is surrounded by infalling neutral hydrogen gas.

For all models, the radiation comes out predominantly blue shifted (Fig. 5). This has profound consequences for its detectability, as radiation blueward of the Ly $\alpha$  line is subject to IGM absorption, an effect that increases rapidly with redshift ( $e^{-\tau} \propto (1+z)^{-8}$  for  $z \geq 4$  (see also eq. 14). For the continuous cooling cases the spectra generally consist of two peaks (Fig. 5), with the exact location of the faint red peak as a good measure of the infall velocity of the gas (Fig. 7). For the central cases, the spectra are generally more dominated by the blue peak and systematically more blueshifted than for the continuous models, with velocity offsets in the range  $\sim 500 - 3000$  km s $^{-1}$  (Fig. 5). The surface brightness profiles are flat (with  $\partial \ln F / \partial \ln \theta \sim -1$  to  $-0.5$ ) for the continuous cooling cases. The exact steepness depends on how centrally concentrated the emission is, rendering the profiles much steeper for the central cases (Fig. 11). We provide explanations for all trends that were seen among the models, involving the surface brightness profiles, the morphology of the blue and red peak, and their relative prominence. For reasons we explain in detail, the surface brightness profile for the continuous cases is significantly more centrally concentrated for its bluest than for its reddest 15% of the photons, which provides a simple observational diagnostic (Fig. 12).

The 'fluorescent' (or 'self-ionized') cases (§ 7) relate to models in which an ionizing source was inserted in the center of the collapsing gas cloud. If the gas sphere is only partially ionized, the fluorescent cases may be viewed as an intermediate stage between the central and continuous models. When the gas becomes fully ionized, the emerging spectra change drastically (Fig. 13). In these cases, we found the line widths in the spectrum to be a good measure for the velocity distribution of the gas, despite the fact that in some cases each Ly $\alpha$  photon may be scattered up to  $10^3 - 10^4$  times. We caution that for these optically thin cases, infall models have almost the same spectrum as outflow models. The only difference is that for infall/outflow the emission line is shifted in frequency to the blue/red, respectively (Fig. 14), by an amount which decreases with the brightness of the central ionizing source. The surface brightness profiles are the same (which was also found by ZM02). The recent Ly $\alpha$  data presented by Weidinger et al. (2004, 2005) may therefore also be consistent with the gas streaming outwards.

Because of the increasing opacity of the IGM with redshift, we expect the Ly $\alpha$  fluxes from high redshift ( $z \gtrsim 4.0$ ) collapsing protogalaxies to be very weak, unless the intrinsic Ly $\alpha$  luminosity is very high. In Paper II, we will present detailed applications of our models to observations of Ly $\alpha$  emitters.

Ongoing and future surveys of Ly $\alpha$  emitters are providing us with useful constraints on the early stages of galaxy formation. We hope the work presented in this paper can contribute to the interpretation of recent and of forthcoming observations of Ly $\alpha$  emitting galaxies.

We thank Mike Shara for suggesting to consider deuterium, Jim Applegate for numerous insightful comments, and Adam

Lidz, Martin Rees, and Rashid Sunyaev for useful discussions. The majority of the calculations were carried out on Beowulf (Groningen Intel Cluster). MD thanks the Kapteyn Astronomical Institute, and ZH thanks the Eötvös University in Budapest, where part of this work was done, for their hospitality. ZH gratefully acknowledges partial support by the National Science Foundation through grants AST-0307291 and AST-0307200, by NASA through grants NNG04GI88G and NNG05GF14G, and by the Hungarian Ministry of Education through a György Békésy Fellowship.

## REFERENCES

- Adams, T. F. 1971, *ApJ*, 168, 575  
 —, 1972, *ApJ*, 174, 439  
 Ahn, S., Lee, H., & Lee, H. M. 2000, *Journal of Korean Astronomical Society*, 33, 29  
 —, 2002, *ApJ*, 567, 922  
 Ajiki, M., Taniguchi, Y., Fujita, S. S., Shioya, Y., Nagao, T., Murayama, T., Yamada, S., Umeda, K., & Komiyama, Y. 2003, *AJ*, 126, 2091  
 Alam, S. M. K., & Miralda-Escudé, J. 2002, *ApJ*, 568, 576  
 Avery, L. W., & House, L. L. 1968, *ApJ*, 152, 493  
 Barkana, R. 2004, *MNRAS*, 347, 59  
 Barkana, R., & Loeb, A. 2003, *Nature*, 421, 341  
 —, 2004, *ApJ*, 601, 64  
 Bertschinger, E. 1985, *ApJS*, 58, 39  
 Birnboim, Y., & Dekel, A. 2003, *MNRAS*, 345, 349  
 Blumenthal, G. R., Faber, S. M., Primack, J. R., & Rees, M. J. 1984, *Nature*, 311, 517  
 Bunker, A., Smith, J., Spinrad, H., Stern, D., & Warren, S. 2003, *Ap&SS*, 284, 357  
 Burles, S., & Tytler, D. 1998, *ApJ*, 499, 699  
 Cantalupo, S., Porciani, C., Lilly, S. J., & Miniati, F. 2005, *ApJ*, 628, 61  
 Cen, R., Haiman, Z., & Mesinger, A. 2005, *ApJ*, 621, 89  
 Chang, E. S., Avrett, E. H., & Loeser, R. 1991, *A&A*, 247, 580  
 Charlot, S., & Fall, S. M. 1993, *ApJ*, 415, 580  
 Christensen, L. 2005, Ph.D. Thesis  
 Cox, A. N. 2000, *Allen's astrophysical quantities* (Allen's astrophysical quantities, 4th ed. Publisher: New York: AIP Press; Springer, 2000. Edited by Arthur N. Cox. ISBN: 0387987460)  
 Dawson, S., Rhoads, J. E., Malhotra, S., Stern, D., Dey, A., Spinrad, H., Jannuzi, B. T., Wang, J., & Landes, E. 2004, *ApJ*, 617, 707  
 Dijkstra, M., Haiman, Z., Rees, M. J., & Weinberg, D. H. 2004, *ApJ*, 601, 666  
 Dijkstra, M., Haiman, Z., & Spaans, M. 2005, *ApJ*, submitted (paper II)  
 Fall, S. M., & Rees, M. J. 1985, *ApJ*, 298, 18  
 Fardal, M. A., Katz, N., Gardner, J. P., Hernquist, L., Weinberg, D. H., & Davé, R. 2001, *ApJ*, 562, 605  
 Field, G. B. 1959, *ApJ*, 129, 551  
 Giovanardi, C., Natta, A., & Palla, F. 1987, *A&AS*, 70, 269  
 Haiman, Z. 2004, *Nature*, 430, 979  
 Haiman, Z., & Quataert, E. 2004, *The Formation and Evolution of the First Massive Black Holes* (ASSL Vol. 308: Supermassive Black Holes in the Distant Universe), 147–  
 Haiman, Z., & Rees, M. J. 2001, *ApJ*, 556, 87  
 Haiman, Z., Spaans, M., & Quataert, E. 2000, *ApJ*, 537, L5  
 Hansen, M., & Oh, S. P. 2005, *MNRAS*, submitted  
 Harrington, J. P. 1973, *MNRAS*, 162, 43  
 Hu, E. M., Cowie, L. L., Capak, P., McMahon, R. G., Hayashino, T., & Komiyama, Y. 2004, *AJ*, 127, 563  
 Hummer, D. G. 1962, *MNRAS*, 125, 21  
 Keres, D., Katz, N., Weinberg, D. H., & Dave, R. 2004, *MNRAS*, submitted  
 Kodaira, K., Taniguchi, Y., Kashikawa, N., Kaifu, N., Ando, H., Karoji, H., Ajiki, M., Akiyama, M., Aoki, K., Doi, M., Fujita, S. S., Furusawa, H., Hayashino, T., Imanishi, M., Iwamura, F., Iye, M., Kawabata, K. S., Kobayashi, N., Kodama, T., Komiyama, Y., Kosugi, G., Matsuda, Y., Miyazaki, S., Mizumoto, Y., Motohara, K., Murayama, T., Nagao, T., Nariai, K., Ohta, K., Ohya, Y., Okamura, S., Ouchi, M., Sasaki, T., Sekiguchi, K., Shimasaku, K., Shioya, Y., Takata, T., Tamura, H., Terada, H., Umemura, M., Usuda, T., Yagi, M., Yamada, T., Yasuda, N., & Yoshida, M. 2003, *PASJ*, 55, L17  
 Kunth, D., Mas-Hesse, J. M., Terlevich, E., Terlevich, R., Lequeux, J., & Fall, S. M. 1998, *A&A*, 334, 11  
 Lee, J. 1974, *ApJ*, 192, 465  
 Lidz, A., Hui, L., Zalardriaga, M., & Scoccimarro, R. 2002, *ApJ*, 579, 491  
 Loeb, A., & Rybicki, G. B. 1999, *ApJ*, 524, 527  
 Madau, P. 1995, *ApJ*, 441, 18  
 Malhotra, S., & Rhoads, J. E. 2002, *ApJ*, 565, L71  
 Maller, A. H., & Bullock, J. S. 2004, *MNRAS*, 471

- Matsuda, Y., Yamada, T., Hayashino, T., Tamura, H., Yamauchi, R., Ajiki, M., Fujita, S. S., Murayama, T., Nagao, T., Ohta, K., Okamura, S., Ouchi, M., Shimasaku, K., Shioya, Y., & Taniguchi, Y. 2004, *AJ*, 128, 569
- McDonald, P., Miralda-Escudé, J., Rauch, M., Sargent, W. L. W., Barlow, T. A., & Cen, R. 2001, *ApJ*, 562, 52
- Neufeld, D. A. 1990, *ApJ*, 350, 216
- . 1991, *ApJ*, 370, L85
- Osterbrock, D. E. 1962, *ApJ*, 135, 195
- Ouchi, M., Shimasaku, K., Akiyama, M., Sekiguchi, K., Furusawa, H., Okamura, S., Kashikawa, N., Iye, M., Kodama, T., Saito, T., Sasaki, T., Simpson, C., Takata, T., Yamada, T., Yamanoi, H., Yoshida, M., & Yoshida, M. 2005, *ApJ*, 620, L1
- Partridge, R. B., & Peebles, P. J. E. 1967, *ApJ*, 147, 868
- Press, W. H., Teukolsky, S. A., Vetterling, W. T., & Flannery, B. P. 1992, *Numerical recipes in FORTRAN. The art of scientific computing* (Cambridge: University Press, |c1992, 2nd ed.)
- Rees, M. J., & Ostriker, J. P. 1977, *MNRAS*, 179, 541
- Rhoads, J. E., & Malhotra, S. 2001, *ApJ*, 563, L5
- Rhoads, J. E., Malhotra, S., Dey, A., Stern, D., Spinrad, H., & Jannuzi, B. T. 2000, *ApJ*, 545, L85
- Rhoads, J. E., Xu, C., Dawson, S., Dey, A., Malhotra, S., Wang, J., Jannuzi, B. T., Spinrad, H., & Stern, D. 2004, *ApJ*, 611, 59
- Rybicki, G. B., & Lightman, A. P. 1979, *Radiative processes in astrophysics* (New York, Wiley-Interscience, 1979. 393 p.)
- Songaila, A., & Cowie, L. L. 2002, *AJ*, 123, 2183
- Spiegel, D. N., Verde, L., Peiris, H. V., Komatsu, E., Nolte, M. R., Bennett, C. L., Halpern, M., Hinshaw, G., Jarosik, N., Kogut, A., Limon, M., Meyer, S. S., Page, L., Tucker, G. S., Weiland, J. L., Wollack, E., & Wright, E. L. 2003, *ApJS*, 148, 175
- Steidel, C. C., Adelberger, K. L., Shapley, A. E., Pettini, M., Dickinson, M., & Giavalisco, M. 2000, *ApJ*, 532, 170
- Thoul, A. A., & Weinberg, D. H. 1995, *ApJ*, 442, 480
- . 1996, *ApJ*, 465, 608
- Unno, W. 1952, *PASJ*, 4, 100
- . 1955, *PASJ*, 7, 81
- Weidinger, M., Møller, P., & Fynbo, J. P. U. 2004, *Nature*, 430, 999
- Weidinger, M., Møller, P., Fynbo, J. P. U., & Thomsen, B. 2005, *A&A*, 436, 825
- Zheng, Z., & Miralda-Escudé, J. 2002, *ApJ*, 578, 33

APPENDIX A  
TESTS OF THE CODE

A.1. *Testing Core Scattering*

The test discussed in § 3.2 mainly addresses scattering of photons in the wing, since  $> 99\%$  and  $> 99.98\%$  of the photons that emerge from the optically thick sphere are in the wings, for  $\tau_0 = 10^5$  and  $10^7$ , respectively. To calculate these numbers, the transition from core to wing was defined at  $|x| = 3$ . Therefore, the emerging spectrum is insensitive to the performance of the code for scatterings in the core. Note that this is exactly why it is allowed to deploy the accelerated scheme (§ 3.1.1) to calculate emerging Ly $\alpha$  spectra from optically thick media. To test the accuracy of the code for scatterings in the core we compare the redistribution function,  $q_{II}(x, x')$  (§ 2), as extracted from the code, with the theoretical solutions given by Hummer (1962) and Lee (1974) (their  $q_{IIb}(x, x')$ ). In the *upper right panel* of Figure 2 we show the cases with  $x = 0$ ,  $x = 2$  and  $x = 5$ . The agreement between the histograms generated by the code, and the theoretical curves is excellent.

An additional test for core scatterings involves the well studied problem of the mean number of scatterings a Ly $\alpha$  photon undergoes,  $\bar{N}$ , before it escapes from the slab (see Adams 1972). To calculate the average number of scatterings a Ly $\alpha$  photon undergoes in our code, we use the weighting scheme described by Avery & House (1968). This weighing procedure reduces the average number of scatterings by a factor of  $\sim 2$ . The main reason is that the distribution of the number of scatterings has a long tail to large number of scatterings, which increases  $\bar{N}$ . The weighting scheme described by Avery & House (1968), gives less weight to the photons that are in the high- $N$  tail, which brings the number of scatterings of individual photons closer to the mean. The filled dots in the *lower left panel* denote  $\bar{N}$  as a function of  $\tau_0$  as extracted from our simulation, whereas the solid line is the theoretical prediction by Harrington (1973)  $\bar{N} = 1.61\tau_0$ . The agreement at large  $\tau_0$  is impressive, but breaks down when  $\tau_0 \lesssim 10^5$ , which is in the transition regime between moderate and extreme optical depths.

A.2. *Testing the Code when the Gas is not Static*

To test the validity of the code in a case when the gas has bulk motions, we compare our results with LR99, who used a Monte Carlo method to calculate the Ly $\alpha$  transfer through a fully neutral, homogeneous, uniform intergalactic medium that undergoes Hubble expansion. They demonstrated that ionizing sources prior to reionization, are embedded in large Ly $\alpha$  halos that are redshifted relative to the host galaxy. Initially, resonant scattering moves the Ly $\alpha$  photons into both the red and blue wing of the line profile, which dramatically increases their mean free path (as discussed in § 2). The increased mean free path enables Hubble expansion to redshift the Ly $\alpha$  photons during their flight. The blue photons return to the line core, while the red photons become even redder. The Ly $\alpha$  photons that have redshifted far enough from the line center stream freely to the observer. LR99 use a simple Monte Carlo approach to calculate the spectrum (their Fig. 2) and surface brightness profiles (their Fig. 1) of these Ly $\alpha$  halos. We quantify this below:

A photon initially at frequency  $x$  (in this case  $x \ll 0$ ), propagating through an expanding IGM, redshifts in proportion to its traversed distance,  $dx = -H(z)ds/v_{\text{th}}$ . Here,  $H(z)$  is the Hubble parameter at redshift  $z$ ,  $ds$  is the differential traversed physical distance, and  $v_{\text{th}}$  is the thermal velocity of the atoms in the IGM. As the photon redshifts, its mean free path increases, and consequently Hubble expansion redshifts the photon even further, etc. The maximum optical depth a photon initially at frequency  $x$  can see through a uniform IGM is given by:

$$\begin{aligned} \tau_x &= \int_0^\infty ds n_H(s)\sigma(s) = n_H\sigma_0 \int_0^\infty ds \phi(x'[s]) = \frac{n_H\sigma_0}{\sqrt{\pi}} \int_0^\infty ds \frac{a}{x'^2[s]} \\ &= \frac{-n_H\sigma_0 v_{\text{th}} a}{H(z)\sqrt{\pi}} \int_x^{-\infty} \frac{dx'}{x'^2} = \frac{-n_H\sigma_0 a v_{\text{th}}}{\sqrt{\pi} H(z) x} \end{aligned} \quad (\text{A1})$$

For  $T = 10^{\circ}\text{K}$ ,  $z = 10$ , and the *WMAP* cosmological parameters,

$$\tau_x \approx \frac{-3.8 \times 10^3}{x} \equiv \frac{x_*}{x}, \quad (\text{A2})$$

in which  $x_*$  is the ‘critical’ frequency, which marks the frequency beyond which the neutral IGM is optically thin. Photons with  $x \ll x_*$  (note that  $x$  is negative) stream freely through the neutral IGM towards the observer. LR99 define their frequency variable in terms of this critical frequency as:  $\hat{x} \equiv x/x_*$ . Note that blue- and redshifted photons have a negative and positive  $\hat{x}$ , respectively.

We caution that the results presented in LR99 are not exactly adequate to test our code in the case of bulk motions. In LR99 the Ly $\alpha$  photons redshift during their flight, while the energy before and after scattering is equal (i.e.  $x_o = x_i$ ). In the case the shells have bulk motion, the photon’s energy changes in a scattering event according to (eq. 3), while the photon’s energy remains constant during its flight. For example: A photon is emitted at  $x = 0$  and  $r = 0$  in the direction  $\vec{k}$ . Consider the situation in which each scattering leaves  $\vec{k}$  unchanged. In LR99, the photon continuously redshifts in between fully coherent scatterings. In the situation in which the gas shells are radially expanding (according to Hubble’s law), the photons frequency will remain the same,  $x = 0$ . Note that the mean free path of this photon is the same in both situations. This photon emerges at a hypothetical boundary in the same number of scatterings in both cases, but in LR99 it is redder. The situation sketched above is very rare, but it is easy to convince oneself that *any* photon, along an arbitrary trajectory, emerges slightly redder in LR99’s scenario. In practice, this difference is small, but leaves a noticeable difference in the spectrum.

LR99 clearly describe their Monte Carlo simulation, which can easily be reproduced and adequately modified to describe Ly $\alpha$  transfer through gas radially expanding outwards from  $r=0$  according to the Hubble law,  $v_{\text{bulk}} = H r$ , where  $H$  is the Hubble constant. The calculated spectrum for this modified LR99 simulation is slightly bluer than their original spectrum shown in *their* Figure 2. This modified curve is shown in the *lower right panel* of our Figure 2 as the *green–solid* line. Note that LR99 used dimensionless units, with all cosmological parameters scaled out. The histogram shown was computed with our own code. Ly $\alpha$  photons were injected in the center of a sphere in which the shells are expanding outwards according to Hubble’s law,  $v_{\text{bulk}} = H(z) r$ . In our code, the variables are not dimensionless. We pick  $z_s = 10$  (which is the physical model LR99 translate their results to) and the density of the gas shells is uniform and  $n_H \sim 2 \times 10^{-7} (1+z_s)^3 \text{ cm}^{-3}$ . The gas temperature was set to 10 K ( $a = 1.5 \times 10^{-2}$ , although the exact temperature barely matters). To facilitate comparison with LR99, this plot uses their frequency variable,  $\hat{x} \sim -3.8 \times 10^3 x$ . As the figure shows, the agreement is excellent.

## APPENDIX B

### ANALYTIC SOLUTION FOR A STATIC UNIFORM SPHERE

In this Appendix we derive an analytic solution for the Ly $\alpha$  spectrum emerging from a uniform, static sphere of gas, similar to the well known solution for a plane–parallel slab derived by Harrington (1973) and Neufeld (1990). Following Harrington (1973); Neufeld (1990), our starting point is the radiative transfer equation after having made the Eddington approximation. In spherical coordinates this reads:

$$\begin{aligned} \frac{\partial^2 J(r, x)}{\partial r^2} + \frac{2}{r} \frac{\partial J(r, x)}{\partial r} &= 3\phi^2(x)\kappa_0^2(J(r, x) - 3\phi(x)\kappa_0^2 L(r)), \\ L(r) &= \int_{-\infty}^{\infty} \phi(x')q(x, x')J(x', r)dx' + \phi(x)\frac{j(r)}{4\pi}. \end{aligned} \quad (\text{B1})$$

Harrington (1973) showed that the integral operator can be written as a differential operator, after applying the *Fokker-Planck approximation*:

$$\int_{-\infty}^{\infty} \phi(x')q(x, x')J(x', r)dx' \approx \phi(x)J(x, r) + \frac{1}{2} \frac{\partial}{\partial x} \phi(x) \frac{\partial J(x, r)}{\partial x}. \quad (\text{B2})$$

After defining the variable  $\sigma$ , by  $\partial x / \partial \sigma = (3/2)^{1/2} \phi(x)$  (note that in the line wing,  $\phi(x) = a / [\pi^{1/2} x^2]$ , and therefore  $\sigma = (2\pi/27)^{1/2} x^3 / a$ ), the transfer equation simplifies to:

$$\frac{\partial^2 J(r, x)}{\partial r^2} + \frac{2}{r} \frac{\partial J(r, x)}{\partial r} + \kappa_0^2 \frac{\partial^2 J(r, x)}{\partial \sigma^2} = -3\phi^2(x)\kappa_0^2 \frac{j(r)}{4\pi}. \quad (\text{B3})$$

Following Unno (1955), this equation is solved using the *Sturm-Liouville* expansion which consists of an eigenfunction expansion of the form:

$$J(r, x) = \sum_{n=1}^{\infty} E_n(r)h_n(x). \quad (\text{B4})$$

Each eigenfunction,  $E_n(r)$ , obeys the following differential equation:

$$\frac{\partial^2 E_n(r)}{\partial r^2} + \frac{2}{r} \frac{\partial E_n(r)}{\partial r} + \lambda^2 E_n(r) = 0 \rightarrow E_n(r) = C \frac{\sin \lambda r}{\lambda r} + D \frac{\cos \lambda r}{\lambda r}, \quad (\text{B5})$$

where  $C$  and  $D$  are arbitrary constants. Note that to prevent the solution from diverging at  $r=0$ ,  $D=0$ . The value of  $\lambda$  is obtained from the boundary condition. As in Unno (1955); Harrington (1973); Neufeld (1990), the flux can be written as:

$$F(r, x) = -\frac{4}{3\kappa_0\phi(x)} \frac{\partial J(x, r)}{\partial r}. \quad (\text{B6})$$

At the boundary, where the radius is denoted by  $r=R$ , all photons are propagating outwards, i.e. no photons get scattered back through the surface. In this case, the flux  $F(R, x) = 2J(R, x)$ . For this equality isotropy, i.e.  $b(r) = 0$ , was assumed. Each function  $E_n(r)$  should obey the boundary conditions, which gives the following constraint on  $\lambda$ :

$$\begin{aligned} \lambda \cot \lambda R &= -\frac{3}{2}\phi(x) + \frac{1}{R} \\ \rightarrow \lambda_n &= \frac{1}{R} \pi n \left( 1 - \frac{2}{3\phi(x)\kappa_0 R + 2} + O[1/(3\phi(x)\kappa_0 R + 2)^2] \right), \\ n &= 1, 2, 3, \dots \end{aligned} \quad (\text{B7})$$

The sequence of solutions for  $\lambda$  was obtained after making the same approximations as in Unno (1955); Harrington (1973). Solutions with different values of  $n$  are orthogonal. Each  $E_n(r)$  can be normalized by multiplying the function by  $\lambda_n/\sqrt{2\pi R}$ . Then  $J(r, x)$  is:

$$J(r, x) = \sum_{n=1}^{\infty} C_n h_n(x) \frac{\sin \lambda_n r}{\lambda_n r} = \frac{1}{\sqrt{2\pi R}} \sum_{n=1}^{\infty} \frac{\sin(\lambda_n r)}{r} h_n(\sigma). \quad (\text{B8})$$

We substitute this back into the radiative transfer equation (eq. B3). Following Harrington (1973), the function  $3\phi^2(x)$  (which is peaked strongly around  $x = 0$ ) is replaced by  $\sqrt{6}\delta(\sigma)$ . The solution for any particular  $h_m(\sigma)$  can be found by multiplying the radiative transfer equation on both sides by the  $m^{\text{th}}$  eigenfunction,  $\sin(\lambda_m r)/r\sqrt{2\pi R}$  followed by integration over  $\int 4\pi r^2 dr$ :

$$\begin{aligned} \kappa_0^2 \frac{\partial^2}{\partial \sigma^2} h_m(\sigma) - \lambda_m^2 h_m(\sigma) &= \frac{-\sqrt{6}\kappa_0^2}{\sqrt{2\pi R}} \frac{\delta(\sigma)}{4\pi} Q_m, \\ Q_m &= \int_0^R 4\pi r^2 dr \frac{\sin(\lambda_m r)}{r} j(r). \end{aligned} \quad (\text{B9})$$

The solution for  $h_m(\sigma)$  is given by:

$$h_m(\sigma) = \frac{\sqrt{6}\kappa_0}{8\pi\sqrt{2\pi R}} Q_m \frac{\exp(-\lambda_m |\sigma|/\kappa_0)}{\lambda_m}, \quad (\text{B10})$$

which in combination with equation (B8) completes the solution for  $J(r, x)$ .

### B.1. Analytic Solution for a Central Source.

First consider the situation in which all photons are emitted at radius  $r_s$ , then:

$$j(r) = \delta(r - r_s), \quad Q_m = \frac{\sin(\lambda_m r_s)}{r_s}, \quad (\text{B11})$$

when substituted into equation (B8) we get:

$$\begin{aligned} J(r, \sigma) &= \frac{1}{\sqrt{2\pi R}} \sum_{n=1}^{\infty} \frac{\sin(\lambda_n r)}{r} \left( \frac{\sqrt{6}\kappa_0}{8\pi\sqrt{2\pi R}} Q_m \frac{\exp(-\lambda_n |\sigma|/\kappa_0)}{\lambda_n} \right) \\ &= \frac{\sqrt{6}}{16\pi^2 R} \frac{\kappa_0}{r r_s} \sum_{n=1}^{\infty} \sin(\lambda_n r) \sin(\lambda_n r_s) \frac{\exp(-\lambda_n |\sigma|/\kappa_0)}{\lambda_n}. \end{aligned} \quad (\text{B12})$$

The spectrum at the boundary is obtained by setting  $r = R$ . From equation (B7) we know:

$$\sin(\lambda_n R) = \cos(\lambda_n R) \frac{\lambda_n R}{1 - 1.5\phi(x)R\kappa_0} \sim (-1)^n \frac{\lambda_n}{1.5\phi(x)\kappa_0}. \quad (\text{B13})$$

Therefore,

$$J(R, \sigma) = \frac{\sqrt{6}}{16\pi^2 R^2} \sum_{n=1}^{\infty} \frac{2\sqrt{\pi}x^2}{3a\kappa_0} (-1)^n \exp\left(\frac{-n\pi |\sigma|}{R \kappa_0}\right) \frac{\sin \lambda_n r_s}{r_s}. \quad (\text{B14})$$

Using

$$\begin{aligned} \sum_{n=1}^{\infty} (-1)^n x^n &= \frac{-x}{1+x}, \quad \text{for } |x| < 1, \\ \cos x &= \frac{e^{ix} + e^{-ix}}{2}, \quad \sin x = \frac{e^{ix} - e^{-ix}}{2i}, \quad \cosh x = \frac{e^x + e^{-x}}{2}, \end{aligned} \quad (\text{B15})$$

we can write:

$$\begin{aligned} J(R, \sigma) &= \frac{\sqrt{6}}{32i\pi^2 R^2 r_s} \frac{2\sqrt{\pi}x^2}{3a\kappa_0} \left( \frac{1}{1 + \exp(\frac{\pi|\sigma|}{R\kappa_0} + i\pi r_s/R)} - \frac{1}{1 + \exp(\frac{\pi|\sigma|}{R\kappa_0} - i\pi r_s/R)} \right) = \\ &= \frac{\sqrt{6}}{48\pi^{3/2} R^2 r_s} \frac{x^2}{a\kappa_0} \left( \frac{\sin(\pi r_s/R)}{\cos(\pi r_s/R) + \cosh(\sqrt{\frac{2\pi^3}{27}} \frac{|x^3|}{aR\kappa_0})} \right). \end{aligned} \quad (\text{B16})$$

When  $r_s \rightarrow 0$ , we obtain (setting  $R\kappa_0 = \tau_0$ )

$$J(r, x) = \frac{\sqrt{6}}{48R^2\sqrt{\pi}} \frac{x^2}{a\tau_0} \left( \frac{1}{1 + \cosh\left(\sqrt{\frac{2\pi^3}{27}} \frac{|x^3|}{a\tau_0}\right)} \right). \quad (\text{B17})$$

The total emerging flux density at the surface can be obtained simply through multiplication by  $4\pi R^2$ . This yields the equation given in equation (9):

$$J(x) = \frac{\sqrt{\pi}}{\sqrt{24}a\tau_0} \left( \frac{x^2}{1 + \cosh\left[\sqrt{\frac{2\pi^3}{27}} \frac{|x^3|}{a\tau_0}\right]} \right) \quad \text{Solution for } sphere, \quad (\text{B18})$$

which can be compared to the previously known analytic solution for a slab (Harrington 1973; Neufeld 1990):

$$J(x) = \frac{\sqrt{6}}{24\sqrt{\pi}a\tau_0} \left( \frac{x^2}{1 + \cosh\left[\sqrt{\frac{\pi^3}{54}} \frac{|x^3|}{a\tau_0}\right]} \right) \quad \text{Solution for } slab. \quad (\text{B19})$$

## APPENDIX C

### DEVIATIONS FROM PARTIAL COHERENCE

In § 2 we mentioned that for all applications discussed in this paper, the scattering is partially coherent. The main reason for this is that the Einstein  $A$  coefficient is very high, which translates to a very short spontaneous decay time,  $t_{\text{spon}} = A_{21}^{-1} = 10^{-8}$  s. Because the hydrogen atoms spend such a short time in the  $n = 2$  state, the chance the atom gets perturbed, while in this excited state, is tiny. Below this is quantified:

#### C.1. Collisions with Electrons

Collisions between the excited hydrogen atom and electrons, can either cause the energy of the re-emitted Ly $\alpha$  photon to differ from that of the incoming photon, or result in the loss of the Ly $\alpha$  photon. The first process occurs when a collision puts the atom in any state from which it radiatively decays back into the  $2p$  state. The last process occurs when the collision puts the atom in a state from which the  $2p$  state is not accessible via a radiative transition. An example of such a state is the  $2s$  level. Osterbrock (1962) gives the collision rate from the  $2p$  to  $2s$  state, at  $T = 10^4$  °K,  $C_{2p2s} \sim 2 \times 10^{-3} n_e \text{ s}^{-1}$ , where  $n_e$  is the number density of electrons. This collision rate dominates the collision rates into all other states by several orders of magnitude (e.g. Giovanardi et al. 1987; Chang et al. 1991). Therefore, only the collision rate from  $2p$  to  $2s$  is relevant for our purposes. Given that the maximum densities in our models reach  $n_e \sim 10^2 \text{ cm}^{-3}$ , the rate at which excited hydrogen atoms get perturbed is at most  $10^{-1} \text{ s}^{-1}$ , which is nine orders of magnitude below the spontaneous decay rate, and therefore negligible.

#### C.2. Absorption of Additional Photons

The Ly $\alpha$  scattering rate for a given hydrogen atom is,

$$P_\alpha = 4\pi \int d\nu \frac{J_\alpha(\nu)\sigma(\nu)}{h\nu} \text{ s}^{-1} \approx \frac{4\pi J_\alpha \sigma_0}{h\nu_0} \nu_0 \frac{v_{\text{th}}}{c} \sim 5 \times 10^{-12} J_{\alpha,21} \text{ s}^{-1}, \quad (\text{C1})$$

where we assumed that  $J(x) = J_\alpha$  is constant and wrote  $J_\alpha = J_{\alpha,21} \times 10^{-21} \text{ ergs s}^{-1} \text{ cm}^{-2} \text{ sr}^{-1} \text{ Hz}^{-1}$ .  $J_{\alpha,21}$  is highest in the central regions in cases in which all Ly $\alpha$  is inserted at  $r = 0$ . An estimate of  $J_{\alpha,21}$  can be obtained from:

$$J_{\alpha,21} = \frac{1}{4\pi\Delta\nu} \frac{L_{\text{Ly}\alpha}}{4\pi r^2} = 3.3 \times 10^7 \left( \frac{L_{\text{Ly}\alpha}}{10^{43} \text{ ergs s}^{-1}} \right) \left( \frac{1 \text{ kpc}}{r} \right)^2 \left( \frac{10^{-4}}{\Delta\nu/\nu_0} \right), \quad (\text{C2})$$

where  $\Delta\nu$  is the line width of the Ly $\alpha$  line, which we set conservatively to  $10^{-4}\nu_0$ . Our lines are typically much broader, which would reduce  $J_\alpha$ . This implies a scattering rate of  $\sim 10^{-4} \text{ s}^{-1}$  at  $r = 1 \text{ kpc}$ . Since the Einstein  $B$ -coefficient for stimulated emission equals that of absorption, the rate at which a hydrogen atom in the excited state absorbs Ly $\alpha$  photons equals that of a hydrogen atom in the ground state. The rate at which stimulated emission of Ly $\alpha$  occurs per hydrogen atom is therefore  $\gtrsim 12$  orders of magnitude lower than  $A_{21}$  for  $r > 1 \text{ kpc}$ , and can be safely ignored.

In the presence of a continuum source, the photo-ionization rate per hydrogen atom from the  $2p$  state by any photon with  $E > 3.4$  eV, emitted by a central source with a powerlaw spectrum  $J(\nu) \propto \nu^{-\beta}$  (for  $h\nu > 3.4 \text{ eV}$ ) is

$$P_{\text{ion}} = 4\pi \int_{3.4 \text{ eV}}^{\infty} d\nu \frac{J(\nu)\sigma_{H\alpha}(\nu)}{h\nu} \text{ s}^{-1} \approx 8 \times 10^{-8} \left( \frac{L_{\text{ion}}}{10^{45} \text{ ergs s}^{-1}} \right) \left( \frac{\beta+1}{\beta+2.75} \right) \left( \frac{10 \text{ kpc}}{r} \right)^2 \text{ s}^{-1}, \quad (\text{C3})$$

where  $\sigma_{H\alpha}(\nu)$  is the photo-ionization cross section from the  $n = 2$  state at frequency  $\nu$ , which is  $\sim 1.4 \times 10^{-17} (\nu/\nu_{H\alpha})^{-2.75}$ , where  $h\nu_{H\alpha} = 3.4 \text{ eV}$  (e.g. Cox 2000, p.108). The total luminosity of the source is given by  $L_{\text{tot}}$ . Photo-ionization out of the  $n = 2$  state by continuum photons emitted by the central source is clearly negligible.

The final mechanism by which the atom may be perturbed in its excited state is by absorbing other line photons. Since the Einstein  $A$  coefficients are weaker for all other transitions in hydrogen, the photo-excitation cross section to other levels is less than the Ly $\alpha$  absorption cross section. For the same number density of these other line photons, the photoexcitation rate is less than the Ly $\alpha$  scattering rate calculated above, which was negligible. Therefore, also this process can be safely ignored, which completes our justification for only considering partially coherent scattering (as compared to incoherent scattering).